HIGHLIGHT

Check for updates

A comprehensive review of the chemical and structural behavior of $MgCO_3 \cdot 3H_2O$ nesquehonite: insights into its stability and functionality

B. D. Botan-Neto (ID) and D. Santamaría-Pérez (ID) *

Considering the geological abundance, stability, and pivotal role of nesquehonite ($MgCO_3 \cdot 3H_2O$) within the $MgO–CO_2–H_2O$ system, this review highlights key aspects of this hydrated magnesium carbonate. These include its synthesis process, crystal morphology, the influence of additives, thermal stability, high-pressure behavior, combined effects of pressure and temperature, as well as insights into hydrogen bonding in nesquehonite and related basic and hydrated carbonates. Finally, the review discusses the potential practical applications of nesquehonite. We conclude that an integrated experimental and theoretical approach provides a clear and accessible framework for understanding nesquehonite's structure, properties, and phase behavior, thereby offering valuable insights to guide further research across multiple scientific disciplines.

Introduction

Internal geological processes on Earth require a thorough understanding of the structural stability of carbonate phases.[1] Notably, carbonates represent the largest carbon reservoir in the Earth's crust and are recycled into the mantle through subduction processes, playing a crucial role as carbon stores in the Earth's interior and, consequently, an important role in the deep carbon cycle.[2–4] The most abundant and stable carbonate phases in the Earth's crust are magnesite ($MgCO_3$), calcite ($CaCO_3$), and dolomite ($CaMg(CO_3)_2$), which together account for more than 90% of the carbonates found in this layer.[5–7]

In subduction zones, carbonates are likely to interact with water-rich fluids, underlining the importance of studying hydrated carbonate compounds.[8] This context fosters the interest in exploring the ternary system $MgO–CO_2–H_2O$.

Departamento de Física Aplicada-ICMUV, MALTA Consolider Team, Universitat de València, 46100, Valencia, Spain. E-mail: David.Santamaria@uv.es

Benedito Donizeti Botan-Neto

Benedito Donizeti Botan-Neto received his bachelor's degree in chemistry from the Instituto Federal de Educação, Ciência e Tecnologia de São Paulo (IFSP), Brazil, where he was awarded the Lavoisier Prize. He later obtained his master's degree in Plasma Physics at the Instituto Tecnológico de Aeronáutica (ITA), Brazil. He is currently pursuing a Ph.D. in Physics at the Universitat de València (UV), Spain, with a research focus on hydrated carbonates under high-pressure and high-temperature conditions.

David Santamaría-Pérez

David Santamaría-Pérez received his Ph.D. in Materials Science from the University Carlos III of Madrid in 2006. He is currently a Professor in Applied Physics at the University of Valencia (Institute of Material Science (ICMUV)), where he leads the "Carbonates at Extreme Conditions" research line. Previously, he held postdoctoral positions at the Max Planck Institute of Chemistry, University Complutense of Madrid, University College London, and UCLA, and was an invited researcher at CSEC (Edinburgh) and the University of Frankfurt. A former Marie Curie and Ramón y Cajal fellow, he is involved in experiments that allow rationalizing the structures of minerals and unveiling novel dense phases.

Magnesium carbonates are present in a variety of naturally occurring minerals within the MgO–CO$_2$–H$_2$O system. These include anhydrous magnesite,[9] the hydrated phases barringtonite (MgCO$_3$·2H$_2$O),[10] nesquehonite (MgCO$_3$·3H$_2$O),[11] lansfordite (MgCO$_3$·5H$_2$O),[12] and basic magnesium carbonates such as hydromagnesite (Mg$_5$(CO$_3$)$_4$(OH)$_2$·4H$_2$O),[13] protohydromagnesite (Mg$_5$(CO$_3$)$_4$(OH)$_2$·11H$_2$O),[14] and an unnamed phase (Mg$_5$(CO$_3$)$_4$(OH)$_2$·8H$_2$O).[15] Other related minerals include dypingite and giorgiosite (both Mg$_5$(CO$_3$)$_4$(OH)$_2$·5–6H$_2$O),[14,16] as well as artinite (Mg$_2$(CO$_3$)(OH)$_2$·3H$_2$O).[17] Additionally, a novel hydrate of magnesium carbonate, MgCO$_3$·6H$_2$O, has been recently synthesized in the laboratory.[18] Fig. 1 shows the ternary diagram of the MgO–CO$_2$–H$_2$O system based on molar composition. Aqueous-phase carbonation reactions produce hydrated magnesium carbonates (HMCs), with nesquehonite standing out as the predominant and most stable pure hydrated magnesium carbonate phase under ambient conditions.[19,20]

Nesquehonite was discovered in June 1888 by Mr. Keeley at the Nesquehoning Mine in Pennsylvania, USA, and was subsequently named 'nesquehonite'. The first report on the mineral was published by Genth and Penfield in 1890.[21] Nesquehonite is described in the monoclinic system with the P2$_1$/n space group, exhibiting a pseudo-orthorhombic nature. The unit cell parameters are approximately: a = 7.68–7.71 Å, b = 5.36–5.39 Å, c = 12.00–12.13 Å, with the β angle ranging from 90.40° to 90.45°, and Z = 4.[11,22,23]

The structure of nesquehonite is shown in Fig. 2. Its crystal structure comprises infinite double chains of corner-sharing, distorted [MgO$_6$] octahedra and [CO$_3$] trigonal groups, oriented parallel to the bc-plane. Each [MgO$_6$] octahedron is coordinated to four oxygen atoms from carbonate groups and two from water molecules. The distortion of the octahedra arises primarily from edge-sharing with adjacent carbonate groups, resulting in notably short O–O distances. Each octahedron shares two corners and one edge with three carbonate groups, while each [CO$_3$] unit is linked to three [MgO$_6$] octahedra through two corners and one shared edge. A unique feature of this connectivity is that the oxygen atom shared between two octahedra is also located on the shared edge with a carbonate group. This intimate coupling between polyhedral units contributes to the distortions observed in both the [MgO$_6$] octahedra and [CO$_3$] groups. Beyond the coordinated water molecules, the structure also includes "lattice" water molecules situated between the chains, not directly bonded to a Mg^{2+} cation. These waters form a network of hydrogen bonds that bridge the octahedral chains, providing additional structural stability. The stability and integrity of the nesquehonite framework are sustained through a combination of ionic, covalent, and hydrogen bonding interactions, with hydrogen bonding playing a particularly critical role in linking and stabilizing the structural chains.[23,24]

Based on the widespread interest in MgO–CO$_2$–H$_2$O phases and the abundance and stability of nesquehonite, this work aims to provide a comprehensive overview of this mineral. The paper is organized into several sections: the synthesis process and crystal morphology of nesquehonite are discussed, along with the influence of additives; the thermal stability of nesquehonite is examined through
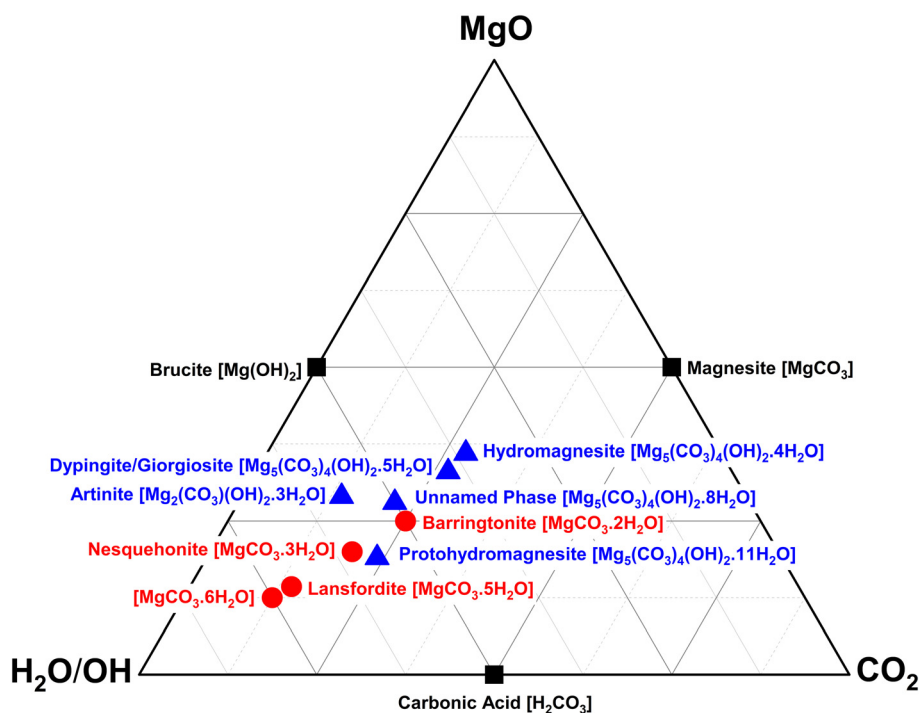

Fig. 1 Ternary diagram of the MgO–CO$_2$–H$_2$O system based on molar composition. Black squares represent the equimolar compounds found in the system, red circles indicate hydrated magnesium carbonates, and blue triangles denote basic magnesium carbonates.
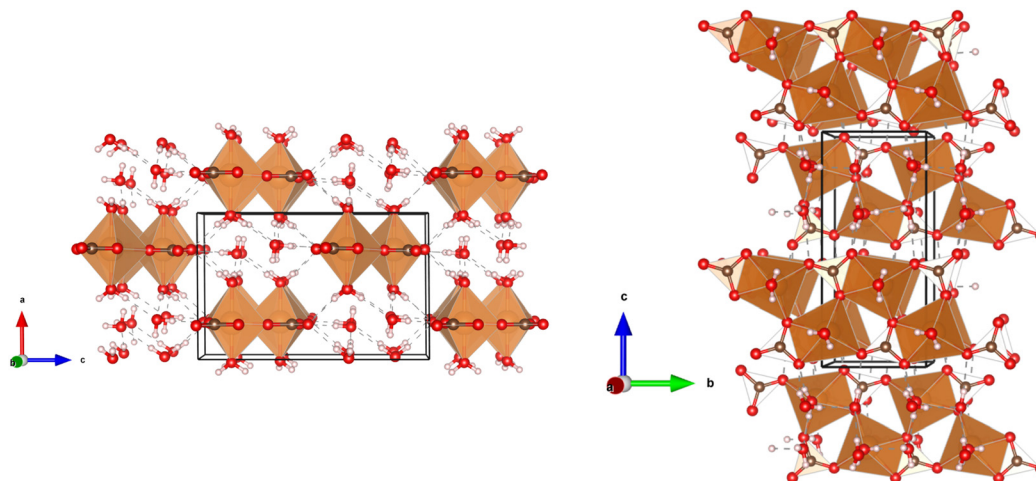
Fig. 2 Projection of $MgCO_3 \cdot 3H_2O$ nesquehonite along the *b*-axis (left) and *a*-axis (right) at room conditions. Magnesium (Mg), oxygen (O), carbon (C), and hydrogen (H) atoms are represented in orange, red, brown, and white, respectively.

Derivative Thermogravimetry (DTG) and Differential Thermal Analysis (DTA) results; high-pressure behavior is then explored using diamond anvil cell (DAC) experiments; the combined effects of pressure and temperature are analyzed; insights into hydrogen bonding in nesquehonite are provided, with comparisons to other basic and hydrated carbonates; and finally, the potential and practical applications of nesquehonite are highlighted.

The MgO–CO₂–H₂O system and the formation of Mg-carbonates

The magnesia–carbonia–water system displays a rich and complex chemistry in which a variety of hydrated and basic magnesium carbonates can form. The hydrated phases are thermodynamically metastable, yet they dominate the assemblages produced at low temperature and near-surface conditions. Thermodynamic calculations demonstrate that, among all known magnesium carbonates, magnesite ($MgCO_3$) is the only phase stable at equilibrium with aqueous solutions containing Mg^{2+} and dissolved CO_2 over a broad range of temperature and pressure. At very low CO_2 partial pressure, brucite is the stable solid, but as CO_2 activity increases, magnesite remains the ultimate equilibrium product. Calorimetric and solubility measurements, coupled with refined thermodynamic models, have firmly established magnesite as the most stable Mg-carbonate under all relevant conditions.[25–27]

Despite its stability, magnesite is notoriously difficult to precipitate at ambient conditions. At 25 °C and moderate CO_2 pressures, direct magnesite crystallization is virtually absent.[28,29] The hydrated carbonate nesquehonite forms readily instead from aqueous solutions.[27] With increasing temperature (typically above 50 °C), precipitation favors basic carbonates such as hydromagnesite, which itself often derives from the transformation of nesquehonite. Experimental work has documented the progressive dehydration of nesquehonite

to hydromagnesite between 50 and 100 °C in the presence of residual water vapor, as we will see later. Formation of anhydrous magnesite requires even more extreme conditions: temperatures of at least 60–100 °C combined with elevated CO_2 pressures, and the process is typically slow, requiring days to weeks at sub-150 °C conditions. Higher salinity, elevated CO_2 fugacity, and lower Mg^{2+} concentration can accelerate dehydration and favor direct magnesite crystallization.[30]

The sequence of phase formation—from highly hydrated carbonates (nesquehonite, lansfordite) to less hydrated ones (hydromagnesite, dypingite) and finally to anhydrous magnesite—illustrates that during crystallization, the system passes through a succession of intermediate, metastable phases before reaching the most stable configuration. The phenomenon reflects the strong hydration of Mg^{2+} ions, which imposes a substantial kinetic barrier to the nucleation of magnesite. Magnesium, as a small divalent cation with high charge density, is surrounded by a tightly bound layer of water molecules, creating around it a hydration shell.[31] Saline environments, by lowering water activity, help destabilize these hydration shells and thus promote dehydration and carbonate crystallization.[32]

In summary, the Mg-carbonate system exemplifies the interplay between thermodynamics and kinetics in mineral formation. Magnesite represents the ultimate stable sink for CO_2, yet its direct precipitation is hindered at Earth-surface temperatures by the strong hydration of Mg^{2+}. As a result, nesquehonite plays a pivotal role as the primary low-temperature carbonate, commonly forming first and serving as a precursor to hydromagnesite and eventually magnesite.

Synthesis and morphological characteristics of nesquehonite

Naturally occurring minerals are fundamental for understanding geological and geochemical processes.

However, their availability is often constrained by natural occurrence, and they typically contain impurities or structural defects that may hinder precise characterization. Consequently, the controlled synthesis of these phases in the laboratory is essential to obtain high-purity materials with well-defined properties, facilitating systematic studies on their crystallographic, thermal, and chemical behavior.

Due to the high hydration capacity of Mg^{2+} ions, HMCs commonly precipitate from bicarbonate-rich aqueous solutions. As aforementioned, this precipitation process is driven by the interaction between Mg^{2+} and HCO_3^- ions and is influenced by various environmental factors, including temperature, hydrogen potential (pH), and partial pressure of CO_2 (pCO_2).[27,33–35] Although nesquehonite was discovered in 1888, artificial crystals of nesquehonite were first synthesized and described by Klaproth in 1808 and later further characterized crystallographically by Marignac in 1855.[21,36]

The most common and widely reported synthesis route for nesquehonite involves the use of magnesium chloride hexahydrate ($MgCl_2 \cdot 6H_2O$),[19,27,37–41] magnesium bicarbonate ($Mg(HCO_3)_2$),[35,42] or magnesium nitrate ($Mg(NO_3)_2$),[43–45] as well as, alternatively, brucite[46–52] as the Mg^{2+} ion source. However, brucite carbonation is complex, as it favors the formation of metastable HMC phases.[51] The carbon source is typically sodium carbonate (Na_2CO_3), although in some cases, a CO_2-rich aqueous environment is employed. Table 1 summarizes literature data on nesquehonite synthesis, highlighting the different magnesium and carbon precursors, as well as the pCO_2 and temperature conditions. The synthesis yield is not reported, as most previous studies do not provide this information in a standardized format or with sufficient detail for reliable comparison.

Simple synthesis routes typically rely on mechanical factors, such as stirring, to dissolve the precursors, leading to the precipitation of nesquehonite, which subsequently undergoes crystallization. Nesquehonite crystals exhibit distinct morphologies, with sharply faceted long needles being the most common (see the specimen obtained by Genth and Penfield[21] in Fig. 3). The morphology of hydrated magnesium carbonates is strongly related to formation conditions—primarily pH and temperature, but also the stoichiometry. The formula $MgCO_3 \cdot xH_2O$ is generally associated with the formation of needle-shaped crystals.[43] However, morphology is not the only parameter influenced by formation conditions. The structural formula of nesquehonite is also highly dependent on the pH of the solution. Two distinct structural formulas have been reported: below pH 8, nesquehonite forms as $Mg(HCO_3)(OH) \cdot 2H_2O$, incorporating bicarbonate (HCO_3^-) and hydroxyl (OH^-) groups into its structure; whereas in the pH range of 8.5 to 12.5, nesquehonite crystallizes as $MgCO_3 \cdot 3H_2O$, containing carbonate (CO_3^{2-}) groups instead.[34,43]

Recently, Back et al.[55] investigated various synthesis approaches for nesquehonite, including production from $MgCl_2$ in the presence of Mg-acetate, synthesis from magnesium sulfate heptahydrate ($MgSO_4 \cdot 7H_2O$) with sodium dodecyl sulfate (SDS), and formation from brucite under high temperature and overpressure CO_2 conditions, aiming to demonstrate the effect of pressure and temperature on nesquehonite crystallization. Their study showed that in the presence of Mg-acetate, nesquehonite formation is consistently favored regardless of the Mg-acetate concentration. However, the size and morphology of the nesquehonite crystals depend strongly on Mg-acetate

Table 1 Summary of literature data on nesquehonite synthesis

| Magnesium precursor	Carbon precursor	pCO_2 (atm)	Temperature (°C)	Reference
$MgCl_2 \cdot 6H_2O$	Na_2CO_3	3.91×10^{-4}	10	37
$MgCl_2 \cdot 6H_2O$	CO_2	1	20	38, 39
$MgCl_2 \cdot 6H_2O$	Na_2CO_3	3.91×10^{-4}	25	53
$MgCl_2 \cdot 6H_2O$	$Na_2CO_3 + CO_2$	9.90×10^{-4}	25	27
$MgCl_2 \cdot 6H_2O$	Na_2CO_3	3.91×10^{-4}	40	37, 40
$MgCl_2 \cdot 6H_2O$	$Na_2CO_3 + C_4H_7NO_4$	3.91×10^{-4}	45	41
$Mg(HCO_3)_2$	CO_2	3.91×10^{-4}	10	35
$Mg(HCO_3)_2$	CO_2	3.91×10^{-4}	60	42
$Mg(NO_3)_2$	HCO_3^-	3.91×10^{-4}	45	44
$Mg(NO_3)_2$	K_2CO_3	3.91×10^{-4}	75	43
$Mg(NO_3)_2$	$(NH_4)_2CO_3$	3.91×10^{-4}	130	45
$Mg(OH)_2$	CO_2	15	20	46
$Mg(OH)_2$	CO_2	0.1	25	47
$Mg(OH)_2$	CO_2	0.5	25	47
$Mg(OH)_2$	CO_2	1	25	47
$Mg(OH)_2$	CO_2	3.91×10^{-4}	28	48
$Mg(OH)_2$	CO_2	1	35	49
$Mg(OH)_2$	CO_2	3.91×10^{-4}	38	48
$Mg(OH)_2$	CO_2	81.2	50	50
$Mg(OH)_2$	CO_2	1	58	52
$Mg(OH)_2$	CO_2	1	70	49
$Mg(OH)_2$	CO_2	15	70	51
$C_8H_{12}MgN_2O_8$	Na_2CO_3	3.91×10^{-4}	45	41
$MgSO_4 \cdot 6H_2O$	Na_2CO_3	3.91×10^{-4}	25	54
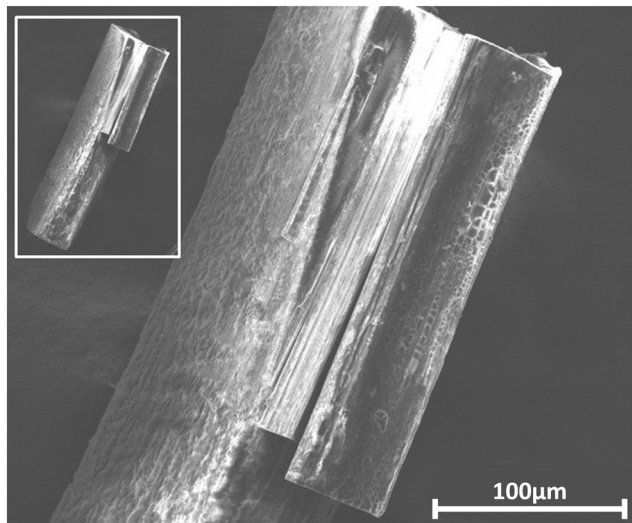
Fig. 3 Scanning Electron Microscope (SEM) image obtained using a high-resolution Hitachi S4800 equipment (scale at the bottom right), showing the characteristic needle-like morphology of a small single crystal of synthetic nesquehonite, provided by the Yale Peabody Museum (specimen YPM MIN 031567). The sample was originally synthesized by Genth and Penfield[21] over a century ago. The inset shows the entire analyzed crystal.

concentration. The aspect ratio of the crystals (defined as the ratio between crystal length and width, serving as a quantitative measure of morphological elongation) increases from 7 to 13 as the Mg-acetate concentration rises to 0.01 M, but decreases with further increases in concentration, dropping to 4 at 1 M Mg-acetate. Similarly, in the presence of SDS, the crystal aspect ratio of nesquehonite increases significantly—from 2.48 to about 5.7 times larger compared to crystals formed without SDS. In this system, the aspect ratio can reach values as high as 26.8, showing a strong effect on crystal morphology like that observed with Mg-acetate.

Finally, aqueous supercritical carbonation of brucite demonstrated that, at 40 °C, large amounts of nesquehonite can be produced across the entire pressure range of 20–100 bars. At 55 °C, however, the process became more pressure-sensitive, producing a nesquehonite-rich hydromagnesite mixture at 100 bars, while strongly favoring hydromagnesite formation at 60 and 20 bars, although nesquehonite was never completely absent in any batch. Comparing the morphology of nesquehonite obtained under these over pressurized conditions with crystals synthesized in the presence of additives reveals that growth occurs from fewer nucleation points, indicating a lower nucleation density than in the Mg-acetate and SDS systems.

Another recent study, conducted by Xu *et al.*,[41] investigated the influence of L-aspartic acid on the morphology, structure, and thermal stability of nesquehonite. The presence of L-aspartate played a crucial role in promoting the formation of thermally stable nesquehonite crystals. The interaction between Mg^{2+} ions and L-aspartate led to the formation of O–Mg complexes, which, in turn, induced the self-assembly of nesquehonite. Under the regulation of

L-aspartate, two competing reactions occur in the system: one involving the interaction between Mg^{2+} and CO_3^{2-} ions, and the other involving Mg^{2+} and the carboxyl functional groups of L-aspartate. The negatively charged carboxylate groups engage in specific interfacial molecular recognition with crystal planes of nesquehonite, providing favorable nucleation sites and facilitating oriented crystal growth. This study offers new insights into how organic molecular additives can direct the mineralization of nesquehonite crystals.

To the best of our knowledge, only a limited number of studies have explored the mechanism of nesquehonite crystal formation from magnesium salts.[37,40,47,50,51,56,57] Recently, Yahyazadeh *et al.*[54] proposed a three-stage crystallization mechanism using magnesium sulfate heptahydrate ($MgSO_4 \cdot 7H_2O$) and sodium carbonate, based on morphological, crystallographic, vibrational, and thermal analyses. The mechanism involves an induction period followed by nucleation, crystal growth, and ripening. During the induction period, nesquehonite nucleation occurs at a very low rate, characterized by a liquid phase that forms immediately after mixing the reactants, resulting in semi-spherical, amorphous nanoparticles with average sizes around 100 nm. In the intermediate stage, corresponding to a semi-solid phase, these amorphous nuclei transform into whisker-like crystals through the formation and stacking of thin, sheet-like structures composed of aggregated nanoparticles, reaching average lengths of approximately 10 μm, although some particles may retain their initial amorphous morphology. The final stage is characterized by a non-Newtonian liquid phase, in which nearly all nanoparticles have disappeared, indicating the completion of nesquehonite crystallization. At this point, only elongated whisker-like crystals remain, with no visible semi-spherical or amorphous particles. Notably, the formation of the intermediate sheet-like structures during the second stage is identified as the rate-determining step in the overall crystallization process.[54]

Thermal stability of nesquehonite

Given the crucial role of carbonates in internal geological processes, understanding their behavior under varying pressure and temperature conditions is essential. As both pressure and temperature increase with depth, the conditions encountered in subduction zones differ significantly from ambient conditions. Over the years, studies have progressively refined our understanding of the thermal stability of nesquehonite, primarily through Derivative Thermogravimetry (DTG) and Differential Thermal Analysis (DTA) measurements. However, discrepancies persist in literature, often attributed to variations in experimental conditions and methodologies—such as heating ramp rates and atmospheric environments.[23,38,58–60] To improve the resolution of the decomposition steps, controlled rate thermal analysis (CRTA) has been employed experimentally.[38]

Nevertheless, to account for these variations and provide a more comprehensive perspective, a literature-based overview of nesquehonite's thermal stability is presented.

Nesquehonite decomposition is commonly described as a two-stage process: dehydration occurring below 300–350 °C, followed by decarbonation above this temperature range. However, nesquehonite undergoes a more complex, multi-step decomposition involving five consecutive stages.[23,38,39,41,44,54,58,59,61–63] Table 2 summarizes selected publications reporting on the thermal decomposition of nesquehonite.

The dehydration stage of nesquehonite consists of three distinct steps. The first step involves the loss of one water molecule, leading to the formation of the so-called "Phase X", a dihydrated magnesium carbonate ($MgCO_3 \cdot 2H_2O$). This transformation is attributed to the release of the non-coordinated water molecule present in the nesquehonite structure. Although Phase X has been identified compositionally, its crystal structure remains unsolved to date. It corresponds to a mass loss of 13(1) wt% and occurs over a temperature range typically starting between 40–70 °C and ending between 117–144 °C, depending on the experimental conditions. Subsequently, the second step involves the loss of an additional water molecule, resulting in the formation of a monohydrated magnesium carbonate ($MgCO_3 \cdot H_2O$). This phase progressively evolves from Phase X and is typically amorphous. It accounts for a mass loss of 12(1) wt% and occurs over a temperature range that starts between 117–144 °C and ends between 183–200 °C. The third step is traditionally considered to involve the release of the final water molecule. However, it is now recognized as a partial dehydration step—a

subject of ongoing debate in literature.[23,58,61] Approximately 0.7 water molecules are lost during this stage, resulting in a compound with an approximate composition of $MgCO_3 \cdot 0.3H_2O$. This step accounts for a mass loss of 9(1) wt% and occurs over a temperature range starting between 183–200 °C and ending between 210–305 °C. With the completion of this step, the dehydration of nesquehonite is considered complete, totaling a mass loss of 34(1) wt% across the three dehydration stages. A representative thermogravimetric model profile built based on literature-reported data is shown in Fig. 4, summarizing the overall decomposition behavior of nesquehonite.

Some studies also report the formation of oxymagnesite ($MgO \cdot 2MgCO_3$), a metastable phase observed as a product of the thermal decomposition of hydrated magnesium carbonates at these temperatures.[23,39] Its crystal structure was theoretically determined via Monte Carlo simulations and later experimentally supported by Rietveld refinement. Its formation was attributed to hypothetical non-equivalent positions of $[CO_3]$ groups in the nesquehonite crystal structure—a feature that would allow one-third of the carbonate groups to release CO_2 at a lower temperature than the remaining $[CO_3]$ groups during thermal treatment.[64–66]

The second stage corresponds to decarbonation, which has mostly been reported to involve the conversion of the magnesite formed in the third step into periclase (MgO), whose structure still contains residual water. This step accounts for a mass loss of 30(2) wt% and occurs over a temperature range of approximately 300–400 °C to 410–476 °C. The fifth and final step consists of the release of the residual water, corresponding to a mass loss of 3.0(5) wt%. The

Table 2 Selected literature data on nesquehonite thermal decomposition at room pressure. Reported parameters include heating ramp, experimental atmosphere, decomposition temperature range, associated mass loss in each step, and identified decomposition products

| Reference	Heating ramp (°C min^{-1})	Atmosphere	Temperature range (°C)	Mass loss (wt%)	Decomposition product
Dell and Weller (1959)[58]	9	Air	25 to 100	26.0	$MgCO_3 \cdot H_2O$
			100 to 305	13.1	$MgCO_3$ (amorphous)
			305 to 410	30.9	MgO
Vágvölgyi et al. (2008)[44]	5	Air	79 to 174	19.3	$Mg(HCO_3)(OH) \cdot H_2O$
			174 to 307	16.1	$Mg(HCO_3)(OH)$
			307 to 449	12.0	$MgCO_3$
			449 to 501	14.5	$MgO + CO_2$ (residual)
			501 to 534	5.0	MgO
Ferrini, De Vito, and Mignardi (2009)[38]	10	—	100 to 200	29.4	$MgCO_3 \cdot H_2O$
			200 to 400	7.8	$MgCO_3$
			400 to 500	31.4	$MgO + CO_2$ (residual)
			500 to 1000	3.9	MgO
Ren et al. (2014)[61]	5, 10, 15, and 20	N_2	40 to 129	14.5	$MgCO_3 \cdot 2H_2O$
			129 to 190	12.6	$MgCO_3 \cdot H_2O$
			190 to 305	7.9	$MgCO_3 \cdot 0.32H_2O$
			305 to 476	31.8	$MgO \cdot 0.32H_2O$
			476 to 600	3.2	MgO
Jauffret, Morrison, and Glasser (2015)[23]	5	N_2	61 to 135	12.5	$MgCO_3 \cdot 2H_2O$
			135 to 185	11.6	$MgCO_3 \cdot H_2O$
			185 to 247	17.8	$MgO \cdot 2MgCO_3$
			363 to 474	28.5	$MgO + CO_2$ (residual)
			474 to 526	3.2	MgO
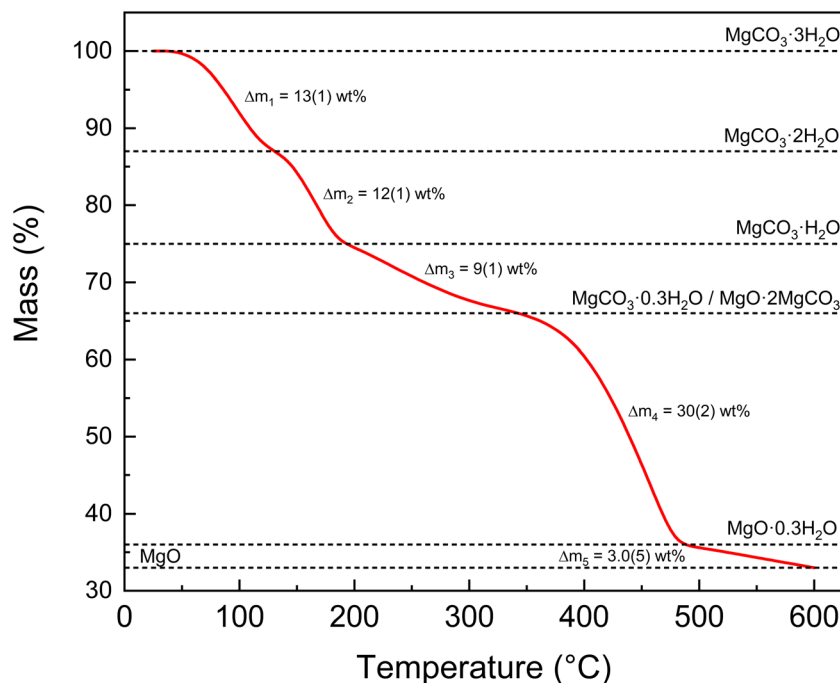
Fig. 4 Representative thermogravimetric model profile of nesquehonite based on literature-reported decomposition steps.

temperature range for this step is reported between 473–487 °C and 510–600 °C. Upon completion of this step, the decarbonation and dehydration processes are considered complete. Overall, the decomposition of nesquehonite results in a total mass loss of 69(4) wt%.

Chaka and Felmy,[67] using density functional theory (DFT) calculations with heat of formation correction (HFC), determined the phase boundary temperatures for nesquehonite at ambient conditions (pCO_2 = 400 ppm and pH_2O = 32 mbar). Their results indicate a transformation of nesquehonite into magnesite + H_2O at −12 °C, and into periclase + CO_2 + H_2O at 57 °C, but kinetic effects seem to play an important role in nesquehonite decomposition.

The morphology of magnesium carbonates is also influenced by the thermal stability of the system. As previously mentioned, nesquehonite predominantly exhibits a needle-like morphology. At lower temperatures (up to 55 °C) and low pH, magnesium carbonate hydrates typically form needle-like crystals, with particle diameter decreasing as temperature and pH increase. At moderately higher temperatures (60–95 °C) and pH values, sheet-like crystallites become the dominant morphology. Further increases in temperature and pH lead to the formation of layered assemblies with diverse morphologies, including rosette-like spherical particles and cake-like aggregates composed of sheet-like units.[43] Structural modifications also affect thermal stability. For instance, Xu et al.[41] demonstrated that the presence of L-aspartic acid enhances the thermal stability of nesquehonite. During the synthesis, L-aspartic acid was carefully added, promoting the incorporation of L-aspartate anions that compete with CO_3^{2-} ions and partially occupy lattice sites at the nesquehonite interface. The exposed cations and anions on the surface of the

nesquehonite crystals interact with L-aspartic acid, resulting in the formation of a layer that acts as a barrier or "protective film" on the crystal surface. As a result, the thermal stability of the nesquehonite crystals is enhanced.[41]

High-pressure behavior of nesquehonite

Given the relevance of carbonates in deep Earth processes (as previously noted), investigating their behavior under high-pressure (HP) conditions is fundamental to understanding carbon cycling in subduction environments. Moreover, the pressure-dependence of the mechanical properties and thermodynamic behavior of hydrated carbonate materials needs to be evaluated. Compared to their thermal stability, the response of nesquehonite to high pressures remains less comprehensively studied. Static high-pressure techniques, such as diamond anvil cells (DACs), offer a powerful means to alter atomic interactions in solids while enabling in situ characterization.[68,69] Under compression, interatomic and intermolecular forces become increasingly repulsive, often leading to phase transitions that minimize the system's free energy. Recent advancements in in situ X-ray diffraction (XRD) have improved our ability to probe structural changes in nesquehonite.[70] This section presents an overview of its structural evolution and high-pressure stability, integrating both experimental and computational findings to elucidate its behavior beyond room conditions.

Recently, Santamaría-Pérez et al.[24] reported the equation of state (EoS) of nesquehonite based on compression experiments conducted in a DAC. Two different pressure-transmitting media (PTMs)—neon and silicone oil—were

used, and the structural evolution was monitored *in situ via* HP synchrotron-based angle-dispersive powder XRD at room temperature. The experimental results were complemented by DFT calculations. The pressure dependence of the unit cell volume and lattice parameters revealed two discontinuities up to 19 GPa, indicating phase transitions at 2.4(2) GPa and 4.0(3) GPa. These transitions correspond to the formation of two distinct high-pressure dense phases, HP1 and HP2. Fig. 5 shows the pressure-induced evolution of nesquehonite's volume per formula unit, measured using neon as the pressure-transmitting medium.

To further investigate these structural changes, two in-house single-crystal XRD (SC-XRD) experiments were performed using a 4:1 methanol–ethanol mixture and paratone oil as PTMs, up to 2.82 GPa. At this pressure, the refined crystal structure remained within the same space group as the initial phase, $P2_1/n$, with lattice parameters exhibiting a small but distinct discontinuity relative to the room pressure nesquehonite structure. The main structural differences arise from slight displacements of the O atoms, which cause the $[CO_3]$ groups to deviate from being perfectly perpendicular to the *a*-axis. As a result, the $[MgO_6]$ octahedra become more distorted.

Later, Botan-Neto *et al.*[71] performed synchrotron-based SC-XRD experiments using helium as the PTM at 3.1 and 11.6 GPa to determine the crystal structures of the HP1 and

HP2 phases. A comparison between the synchrotron SC-XRD data collected at 3.1 GPa (HP1 phase) and previously reported in-house SC-XRD data revealed several weak reflections that had likely been overlooked in the earlier study. Thus, HP1 was indexed in the monoclinic space group $P2_1/c$, with lattice parameters $a = 24.9959(11)$ Å, $b = 7.0883(17)$ Å, $c = 10.3597(5)$ Å, and $\beta = 101.549(4)°$, yielding a unit cell volume of 1798.2(4) Å^3 ($Z = 16$, $\rho = 2.04(3)$ g cm^{-3}). The key difference is that the previously reported phase contained four times fewer crystallographically independent atoms, resulting in fewer orientations of carbonate groups and water molecules. The presence of multiple polymorphs for HP1, differing in water orientations and lying close in energy at distinct local minima of the energy landscape, cannot be ruled out. The HP2 phase at 11.6 GPa was indexed in the $I2/a$ space group, with lattice parameters $a = 9.4473(8)$ Å, $b = 6.748(5)$ Å, $c = 11.8426(11)$ Å, and $\beta = 95.703(6)°$, corresponding to a unit cell volume of 751.2(6) Å^3 ($Z = 8$, $\rho = 2.45(8)$ g cm^{-3}).

Fig. 6a shows the HP1 structure projected along two different crystallographic axes. The HP1 phase retains the fundamental structural topology of the initial nesquehonite, which is characterized by double chains composed of trigonal $[CO_3]$ groups and highly distorted $[MgO_6]$ octahedra running parallel to the *c* axis (equivalent to the *b* axis in initial nesquehonite). The strong distortion of the $[MgO_6]$ units arises from the edge-sharing connectivity with the $[CO_3]$ groups, leading to very short O–O equatorial distances within the octahedra. Two additional equatorial O atoms in each $[MgO_6]$ octahedron are corner-sharing with $[CO_3]$ groups, while the apical O atoms are coordinated to two H$_2$O molecules, forming chains with a stoichiometry of MgCO$_3$·2H$_2$O. An additional "lattice" H$_2$O molecule lies between these double chains, linking them *via* hydrogen bonds.

The orientation of the three water molecules, as well as the number and directionality of O–H hydrogen bonds, impart a distinct structural character to the HP1 phase. The carbonate groups, which are approximately parallel to the *bc* plane in nesquehonite, are tilted in the HP1 phase with respect to the *ac* plane by angles ranging from 3.17° to 10.56°. These tilts result in further distortion of the $[MgO_6]$ octahedra. Moreover, the spatial arrangement of the MgCO$_3$·2H$_2$O chains is significantly modified in the HP1 phase. An analysis of the shortest O–O interchain distances reveals that the chains move closer together in the vertical direction, while becoming more widely separated horizontally, indicating anisotropic compression and structural reorganization under pressure. This coordinated displacement between chains is either driven by—or leads to—an increased number of highly directional hydrogen bonds aligned along the long axis, which likely contribute to the stabilization of the HP1 structure (hydrogen bond details and discussion are provided in the hydrogen bond section).
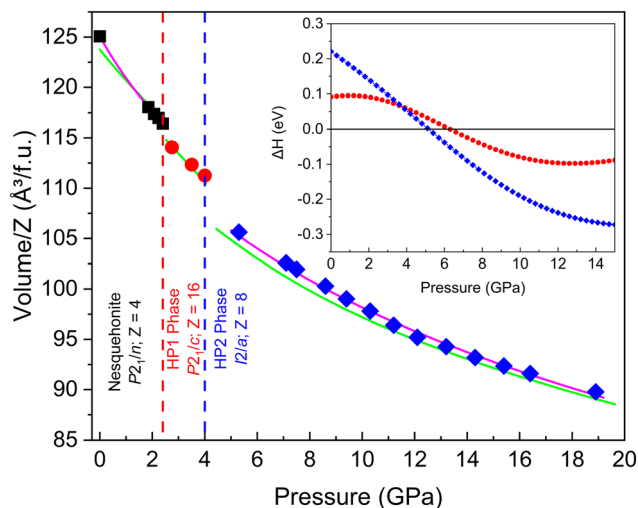

Fig. 5 Pressure dependence of the volume of nesquehonite per formula unit up to 19 GPa, using neon as the pressure-transmitting medium. Black squares, red circles, and blue diamonds correspond to experimental powder data for the nesquehonite, HP1, and HP2 phases, respectively. The solid green line represents DFT results obtained with the B86bPBE functional combined with the exchange-hole dipole moment (XDM) dispersion correction. Solid magenta lines indicate fits to the third-order Birch–Murnaghan equation of state to experimental data. The inset shows DFT-calculated enthalpy variation as a function of pressure for the three polymorphs, using nesquehonite as the reference structure. Estimated standard deviations (ESDs) for the experimental data are smaller than the symbol sizes. Figure adapted from Santamaría-Pérez *et al.*[24] Licensed under CC BY 4.0 (**https://creativecommons.org/licenses/by/4.0/**).
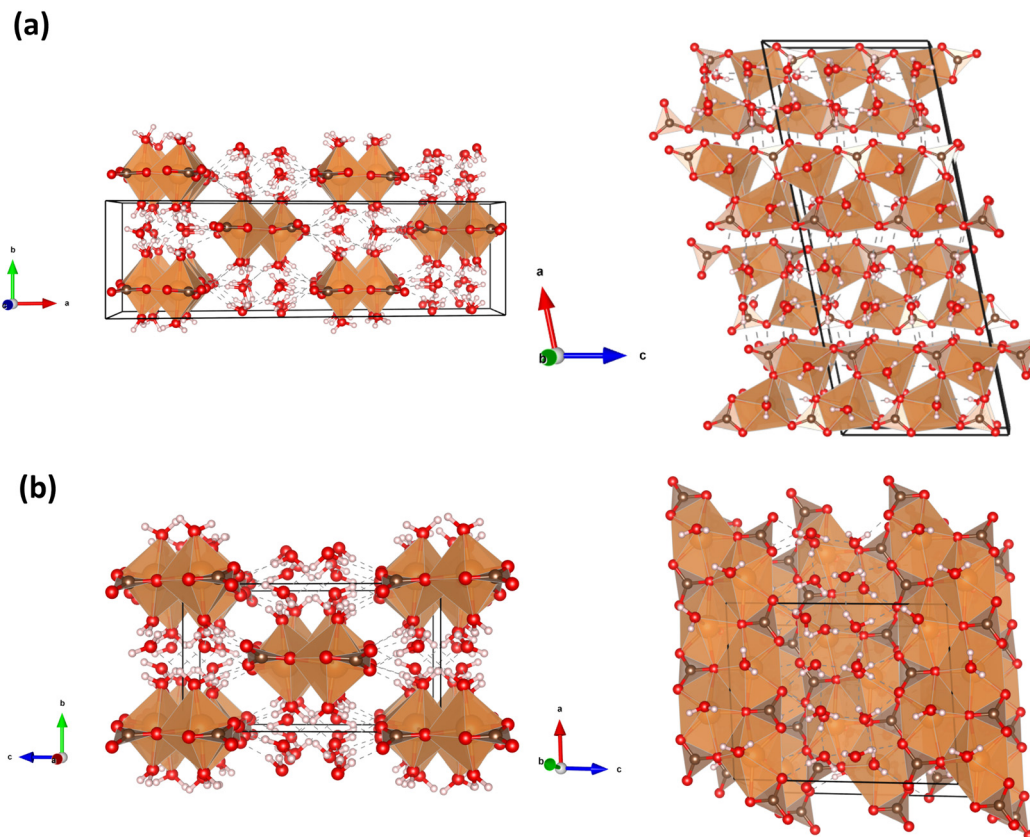
(a)

(b)

Fig. 6 (a) Crystal structure projections of the HP1 phase along the *c*-axis (left) and *b*-axis (right) at 3.1 GPa. (b) Crystal structure projections of the HP2 phase along the *a*-axis (left) and *b*-axis (right) at 11.6 GPa. Magnesium (Mg), oxygen (O), carbon (C), and hydrogen (H) atoms are shown in orange, red, brown, and white, respectively.

Fig. 6b shows the HP2 structure projected along two different crystallographic axes. The HP2 phase also consists of chains with the stoichiometry $MgCO_3·2H_2O$ and includes a "lattice" water molecule located in the interchain space, like the initial nesquehonite and the HP1 phase. However, this second pressure-induced transition is characterized by an increase in the coordination number of Mg atoms from 6 to 7, leading to the formation of distorted $[MgO_7]$ pentagonal bipyramids. Unlike HP1, the carbonate groups in HP2 share two of their edges with equatorial positions of the pentagonal bipyramids. The $[CO_3]$ groups are more tilted relative to the equatorial plane of the chains, with an inclination angle of 21.95°. Once again, hydrogen bonds play a crucial role in linking the polyhedral units within and between chains, as well as the interchain water molecules. An analysis of the shortest O–O interchain distances reveals that the facing chains move closer together, while also adopting a configuration with greater lateral overlap under compression. These structural modifications are associated with the enhanced directionality of the hydrogen bonds along the *c* axis in the HP2 phase.

Third-order Birch–Murnaghan (BM3) EoS parameters were fitted to the *P*–*V* datasets. For nesquehonite, the BM3 fit yielded a zero-pressure unit cell volume (V_0) of 500.3(7) Å³, a bulk modulus (B_0) of 24(2) GPa, and a first pressure

derivative (B_0') of 12(3). These results are in good agreement with DFT calculations, which provided V_0 = 494.8(2) Å³, B_0 = 38.2(5) GPa, and B_0' = 4.43(16). The compressibility of the HP1 phase could not be evaluated due to the limited number and significant dispersion of the available pressure–volume (*P*–*V*) data points. For HP2, the experimental bulk modulus was determined as B_0 = 25.2(12) GPa, with the first pressure derivative fixed to the theoretical value B_0' = 6. DFT calculations yielded a slightly higher value of B_0 = 30.0(2) GPa for this phase.

The anisotropy of both nesquehonite and the HP2 phase was also investigated, revealing pronounced anisotropic compressibility in both structures. In nesquehonite, the *a*-axis is the most compressible, followed by the *b*-axis, while the *c*-axis exhibits a negative axial compressibility. The axial compressibilities estimated from experimental (theoretical) data are: κ_a = 21.6 × 10⁻³ GPa⁻¹ (14.2 × 10⁻³ GPa⁻¹), κ_b = 7.5 × 10⁻³ GPa⁻¹ (6.66 × 10⁻³ GPa⁻¹), and κ_c = −8 × 10⁻³ GPa⁻¹ (2.34 × 10⁻³ GPa⁻¹). In the HP2 phase, the *a*-axis is again the most compressible, followed by the *b*-axis and then the *c*-axis. The corresponding axial compressibilities are: κ_a = 8.5 × 10⁻³ GPa⁻¹ (4.7 × 10⁻³ GPa⁻¹), κ_b = 5.7 × 10⁻³ GPa⁻¹ (5.1 × 10⁻³ GPa⁻¹), and κ_c = 5.0 × 10⁻⁴ GPa⁻¹ (1.3 × 10⁻³ GPa⁻¹).

As previously mentioned, DFT calculations exhibit excellent agreement with the experimental data, as shown in

Fig. 5. Furthermore, DFT results indicate that the nesquehonite-to-HP2 phase transition occurs at approximately 5 GPa (see the enthalpy–pressure graph as inset in Fig. 5), closely matching experimental observations. On the other hand, the calculations suggest that the HP1 phase is a metastable intermediate along the transition pathway to the denser, thermodynamically stable HP2 phase. Consequently, the existence of other metastable phases within the 2.4–4.0 GPa pressure range cannot be ruled out. Additional DFT calculations were also performed to evaluate the energetics of the $MgCO_3 \cdot 3H_2O \rightleftharpoons MgO + 2H_2O + H_2CO_3$ reaction at high pressures. These results demonstrate that the formation of carbonic acid is energetically unfavorable, as the combined enthalpy of the right-hand side of the reaction is more than 0.2 eV higher per formula unit than that of $MgCO_3 \cdot 3H_2O$.

Nesquehonite and its dense polymorphs were also characterized by Raman spectroscopy up to 17 GPa. The Raman spectra of nesquehonite display characteristic peaks in the typical spectral regions of carbonates, which can be divided into three frequency ranges associated with the internal vibrations of the $[CO_3]$ groups and their lattice vibrations involving the cation.[72,73] According to the literature, the most intense Raman peak of nesquehonite is observed around 1100 cm^{-1}, corresponding to the symmetric stretching vibration (v_1) of the carbonate group.[74,75] In the low-frequency region, nesquehonite exhibits several lattice vibration peaks between 119 and 344 cm^{-1}.[56,73] Very weak peaks observed near 707 and 773 cm^{-1} correspond to the in-plane bending mode (v_4) of the carbonate group.[73,76,77]

Raman spectroscopy reveals phase transitions near 2.5 and 4.1 GPa, followed by a region of vibrational instability between 4.1 and 7.8 GPa, during which a continuous transformation into the HP2 phase occurs. The pressure dependence of the Raman-active modes was experimentally

analyzed for the nesquehonite, HP1, and HP2 phases and compared with DFT results. Fig. 7 depicts representative Raman spectra of the three phases—nesquehonite at room pressure, HP1 at 2.5 GPa, and HP2 at 8.9 GPa.

The structural transformations occurring below 5.7 GPa primarily involve changes in the intensity of lattice vibration bands below 260 cm^{-1}. Notably, four lattice vibration modes associated with Mg atoms, observed below 185 cm^{-1} in the nesquehonite spectra at pressures below 2 GPa, soften with increasing pressure, indicating the onset of the transition to the HP1 phase above this range. Following the phase transition, these lattice modes exhibit a slight hardening as pressure increases.

At 5.7 GPa, the Raman spectra show the onset of additional features in the frequency range between 600 and 800 cm^{-1}. Above 7.8 GPa, at least four new Raman bands clearly emerge in the 260–430 cm^{-1} region, along with two additional bands band appearing near ~720 cm^{-1}, which are assigned to the in-plane bending vibration (v_4 mode) of the carbonate group. The increase in intensity of this band appears to be associated with structural changes in the HP2 phase, particularly the sharing of two edges between the $[CO_3]$ group and $[MgO_7]$ pentagonal bipyramids.

XRD experiments and Raman spectroscopy measurements, supported by DFT calculations, are highly complementary and provide a detailed overview of nesquehonite upon compression. While XRD reveals the sequence of phase transitions, Raman spectroscopy not only confirms these transitions but also highlights the emergence of new vibrational modes associated with changes in the coordination environment of Mg atoms.

Coupled effects of pressure and temperature on nesquehonite

Beyond the compression behavior of nesquehonite, Santamaría-Pérez et al.[24] investigated the coupled effects of pressure and temperature on this mineral. The experiments were conducted using resistive heating in a DAC system, which included a heating ring that uniformly heated all components of the DAC to ensure homogeneous temperature distribution across the sample. Silicone oil was used as the PTM. The thermal behavior of nesquehonite was examined at 0.7(1) GPa, with temperatures up to 160 °C, and was monitored in situ using HP synchrotron-based angle-dispersive powder XRD.

Fig. 8 shows the temperature-induced evolution of nesquehonite's XRD patterns at 0.7 GPa. The initial nesquehonite phase remains stable up to 110 °C, where a new phase emerges. The unit cell volume of nesquehonite shows a smooth increase upon heating, with the unit cell axes exhibiting markedly anisotropic behavior, like that previously reported at room pressure.[39] Axial thermal expansion is positive only along the c-axis, which consistently expands upon heating. The experimentally determined thermal expansion coefficients for the c-axis are $\alpha_c = 1.24(2) \times 10^{-3}$ K^{-1}
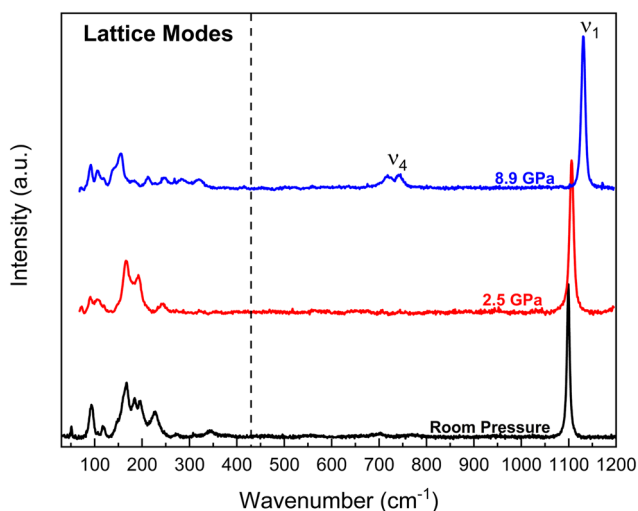

Fig. 7 Room-temperature Raman spectra of nesquehonite polymorphs at room pressure, 2.5 GPa (HP1 phase), and 8.9 GPa (HP2 phase) during compression.
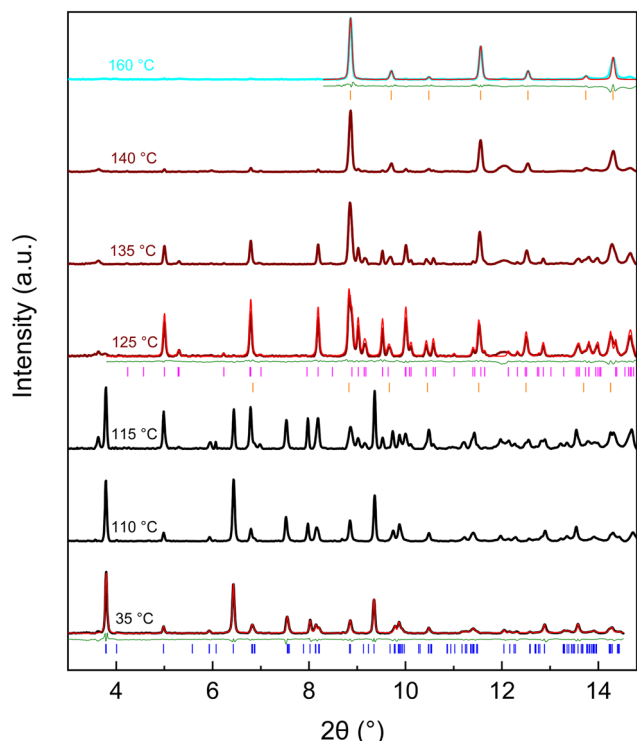
Fig. 8 High-temperature X-ray diffraction patterns of nesquehonite up to 160 °C at 0.7 GPa, measured using silicone oil as the pressure-transmitting medium. The red and olive solid lines represent the Le Bail fits and the difference profiles, respectively. Blue, magenta, and orange vertical ticks indicate the Bragg reflection positions corresponding to nesquehonite, the high-temperature (HT) phase, and magnesite, respectively. Unindexed bands in the patterns, not accounted for by the Le Bail refinement, come from the silicone oil.

at room pressure and $1.06(2) \times 10^{-3}$ K^{-1} at 0.7 GPa. In contrast, the b-axis contracts at high temperature, showing a roughly linear decrease, with thermal expansion coefficients of $\alpha_b = -8.8(13) \times 10^{-5}$ K^{-1} at room pressure and $-9.0(3) \times 10^{-5}$ K^{-1} at 0.7 GPa. The a-axis parameter decreases slightly up to 50 °C and 70 °C for the room pressure and high-pressure runs, respectively, and then begins to increase.

At 115 °C, a new phase appears, while coexisting with nesquehonite. This temperature is close to where the phase transition to Phase X has been reported under room pressure. However, no such transition is observed in that study.[24] The HP-HT phase has a narrow region of stability. At 125 °C no nesquehonite peaks are present. Above this temperature, the intensity of the diffraction peaks of the hydrated HT phase gradually decreases, while other reflections—identified as belonging to MgCO$_3$ magnesite—increase progressively. At 140 °C, the magnesite reflections become very pronounced, and by 160 °C, the XRD pattern is dominated by reflections corresponding to anhydrous magnesium carbonate. In other words, at 0.7 GPa and 160 °C, the newly formed hydrated HT phase undergoes complete dehydration and transforms into MgCO$_3$ magnesite.

The structure of the HT phase could not be definitively identified. However, an indexing procedure was carried out

using 13 reflections collected at 125 °C, yielding an orthorhombic unit cell with lattice parameters $a = 9.183(6)$ Å, $b = 5.736(2)$ Å, and $c = 5.324(6)$ Å, corresponding to a unit cell volume of 280.4(4) Å^3. This solution suggests a volume increase of approximately 14% per formula unit, which may indicate a disproportionation of nesquehonite and the formation of a new phase, MgCO$_3$·4H$_2$O, and magnesite. Upon further heating, this novel HT-hydrated phase gradually releases water molecules, eventually resulting in complete dehydration and transformation into magnesite. The existence of an intermediate phase as a thermal decomposition product of nesquehonite is supported by transitions reported in the literature. However, a direct comparison of d-spacings between this phase and the previously reported "Phase X" evidence that they do correspond to different phases. Likewise, the previously mentioned oxymagnesite[64–66]—formed as a decomposition product of hydrated magnesium carbonates and crystallizing in the cubic space group $I\bar{4}3m$ with lattice parameter $a = 8.5205(1)$ Å—is inconsistent with the observed reflections and the orthorhombic structure tentatively suggested in ref. 24.

Hydrogen bonding in nesquehonite and related hydrated carbonates

Understanding the structural framework of hydrated carbonates requires a detailed analysis of hydrogen bonding interactions.[24] These non-covalent interactions, typically denoted as D–H···A, arise between a hydrogen atom covalently bound to a donor (D) and a nearby acceptor (A). The strength and nature of such bonds are influenced by factors such as the H···A distance and the ∠DHA angle, as schematically illustrated in Fig. 9a. Often found in systems with moderately polar donor groups, hydrogen bonds significantly affect the stability and arrangement of hydrogen-bearing phases. For classification and characterization purposes, the Steiner and Jeffrey criteria offer a widely accepted approach.[71,78–83]

As described earlier, the structure of nesquehonite consists of strongly distorted, corner-sharing [MgO$_6$] octahedra. Each octahedron shares one equatorial edge with a carbonate group and the remaining two equatorial corners with two other carbonate groups, while the apical positions are occupied by two water molecules. An additional non-coordinated "lattice" water molecule resides in the interchain space. These water molecules are responsible for connecting the double chains *via* hydrogen bonding. This structural role and pattern are preserved in the two high-pressure polymorphs of nesquehonite (HP1 and HP2), despite differences in coordination environments—transitioning from [MgO$_6$] octahedra to distorted [MgO$_7$] pentagonal bipyramids in HP2. The primary difference lies in the hydrogen bond directionality, which roughly aligns along the c, a, and c crystallographic axes in nesquehonite, HP1, and HP2, respectively. Fig. 9b–d illustrate the magnesium coordination environments and the interactions between
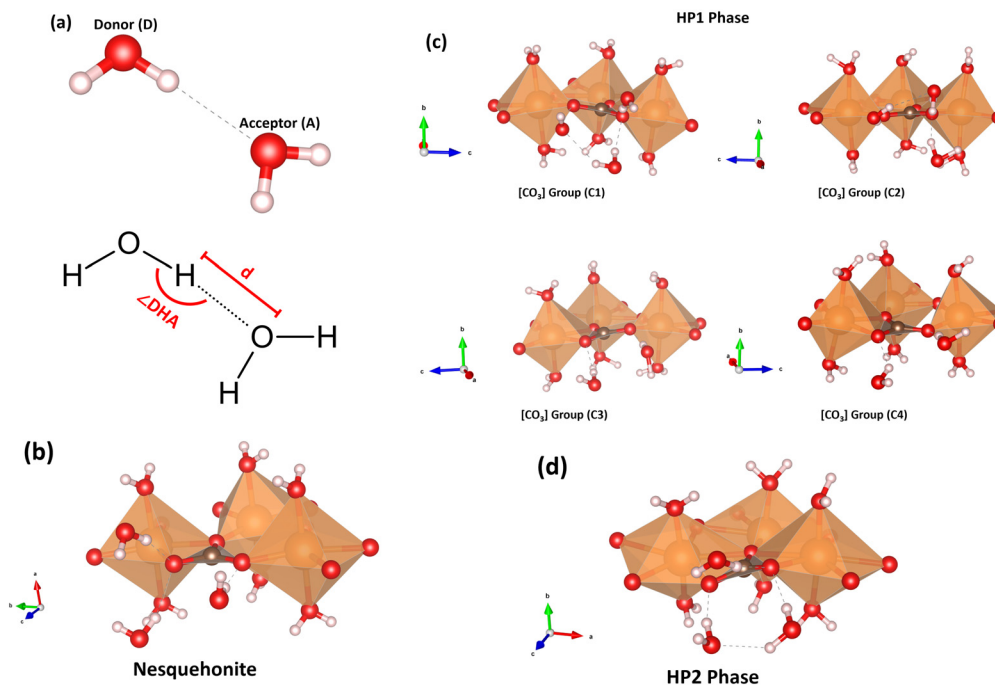
Fig. 9 (a) Schematic representation of a D–H···A hydrogen bond between two water molecules, illustrating the donor (D), acceptor (A), H···A distance, and ∠DHA angle. (b) Nesquehonite [MgO$_6$] coordination and hydrogen bonding. (c) HP1 [MgO$_6$] coordination and hydrogen bonding involving the four independent [CO$_3$] groups. (d) HP2 [MgO$_7$] coordination and hydrogen bonding. Magnesium (Mg), oxygen (O), carbon (C), and hydrogen (H) atoms are shown in orange, red, brown, and white, respectively. Covalent bonds are represented as solid lines, and hydrogen bonds as dashed lines. Figure adapted from Botan-Neto et al.[71] Licensed under CC BY 4.0 (**https://creativecommons.org/licenses/by/4.0/**).

water molecules and carbonate groups in these three phases, highlighting the orientation of the hydrogen bonds. The average H···O distances and ∠DHA angles are 1.96(3) Å and 170(2)° for nesquehonite, 1.90(3) Å and 155(3)° for HP1, and 1.76(5) Å and 160(7)° for HP2. According to the Steiner and Jeffrey criteria, these values classify the hydrogen bonds as moderate in strength, exhibiting ionic character with moderate directionality.

As the investigation of hydrogen bonding is inherently dependent on the resolved crystal structure of each mineral —and considering that only a few hydrated magnesium carbonates (HMCs), such as nesquehonite, lansfordite, hydromagnesite, and artinite, have well-characterized structures—it becomes particularly valuable to extend such studies to other M$_n$O–CO$_2$–H$_2$O systems, where M may be calcium ($n = 1$), sodium ($n = 2$), or even mixed cations. Table 3 summarizes the chemical formula, space group, coordination environment, water position in the Mg polyhedra, and average H···O distances and ∠DHA angles for various hydrated carbonate minerals.

Water position within the polyhedral coordination environment of the selected hydrated carbonates was

Table 3 Summary of hydrogen bonds based on the chemical formula, space group, coordination environment, water position in Mg polyhedra, and average H···O distances and ∠DHA angles for various hydrated carbonate minerals

Mineral name	Chemical formula	Space group	Coordination environment	Water position in polyhedron	H···O (Å)	∠DHA angle (°)	Reference
Nesquehonite	MgCO$_3$·3H$_2$O	$P2_1/n$ (14)	MgO$_6$	Apical	1.96(3)	170(2)	24
Nesquehonite HP1	MgCO$_3$·3H$_2$O	$P2_1/c$ (14)	MgO$_6$	Apical	1.90(3)	155(3)	71
Nesquehonite HP2	MgCO$_3$·3H$_2$O	$I2/a$ (15)	MgO$_7$	Apical	1.76(5)	160(7)	71
Lansfordite	MgCO$_3$·5H$_2$O	$P2_1/c$ (14)	MgO$_6$	Apical/equatorial	1.84(6)	167(5)	84
Artinite	Mg$_2$(CO$_3$)(OH)$_2$·3H$_2$O	$C2/m$ (12)	MgO$_5$ + OH	Apical/equatorial	1.89(6)	166(6)	85
Hydromagnesite	Mg$_5$(CO$_3$)$_4$(OH)$_2$·4H$_2$O	$P2_1/c$ (14)	MgO$_5$ + OH	Apical	1.93(1)	163(1)	13
Monohydrocalcite	CaCO$_3$·H$_2$O	$P3_121$ (152)	CaO$_7$	Apical	1.88(1)	180(1)	86
Ikaite	CaCO$_3$·6H$_2$O	$C2/c$ (15)	CaO$_8$	Apical/equatorial	2.01(2)	170(2)	87
Thermonatrite	Na$_2$CO$_3$·H$_2$O	$P2_1ab$ (29)	NaO$_6$/NaO$_7$	Apical	1.84(1)	164(1)	88
Natron	Na$_2$CO$_3$·10H$_2$O	Cc (9)	NaO$_6$	Apical/equatorial	1.99(5)	163(5)	89
Trona	Na$_3$H(CO$_3$)$_2$·2H$_2$O	$C2/c$ (15)	NaO$_6$	Basal	1.92(3)	171(5)	90
HP trona at 17.9 GPa	Na$_3$H(CO$_3$)$_2$·2H$_2$O	$P\bar{1}$ (2)	NaO$_7$/NaO$_8$	Apical/equatorial	1.77(6)	146(7)	91
Pirssonite	Na$_2$Ca(CO$_3$)$_2$·2H$_2$O	$Fdd2$ (43)	NaO$_7$/CaO$_8$	Apical/equatorial	1.83(3)	177(2)	92
Gaylussite	Na$_2$Ca(CO$_3$)$_2$·5H$_2$O	$C2/c$ (15)	NaO$_6$/CaO$_8$	Apical/equatorial	1.84(1)	171(1)	93

evaluated, revealing no evidence of systematic behavior. Water molecules occupy exclusively apical positions in nesquehonite and its high-pressure polymorphs, as well as in hydromagnesite, monohydrocalcite, and thermonatrite. In contrast, a combination of apical and equatorial sites is observed in lansfordite, artinite, ikaite, natron, high-pressure trona, pirssonite, and gaylussite. Notably, trona is the only structure among those analyzed in which water molecules occupy basal positions of a trigonal prism. Interestingly, nesquehonite and its polymorphs are also the only structures exhibiting non-coordinated water molecules within their crystal framework.

Otherwise, when analyzing the degree of hydration in relation to the hydrogen-bonding network, certain trends and noteworthy structural behaviors can be identified. To begin with, it is essential to define the concept of a hydrogen-bond network within the context of hydrated carbonates. Here, it refers to the spatial arrangement of hydrogen bonds primarily formed between water molecules, carbonate groups, and, in some cases, hydroxyl groups. These interactions collectively contribute to the structural cohesion, stabilization, and connectivity of the crystal lattice.[94–97]

While this definition provides a general framework, the dimensionality of the hydrogen-bonding network must also be considered. A discrete (0D) hydrogen-bond network refers to a non-continuous arrangement in which water molecules form localized interactions with nearby ions, without extending connectivity beyond the immediate coordination environment. A 1D network is characterized by linear or chain-like hydrogen bonds, typically involving water molecules bridging adjacent structural units. A 2D hydrogen-bond network consists of planar arrangements that interconnect structural units within a single crystallographic layer, thereby enhancing cohesion perpendicular to the stacking direction. A 3D hydrogen-bond network involves a fully interconnected framework of hydrogen bonds, extending in all spatial directions and reinforcing the overall integrity of the structure. Finally, cage-like or clustered hydrogen-bond networks are defined by closed or semi-closed groupings of water molecules (e.g., rings or cages), which often surround cations or carbonate groups contributing to the stabilization of metastable or low-temperature phases.

Based on these definitions, the hydrated carbonates analyzed in this work can be classified according to the dimensionality of their hydrogen-bond networks. Fig. 10 illustrates the representative hydrogen-bonding motifs observed in each structure.

Minerals exhibiting 0D hydrogen-bond networks include monohydrocalcite, pirssonite, and thermonatrite, illustrated in Fig. 10a, b and c, respectively. These structures are
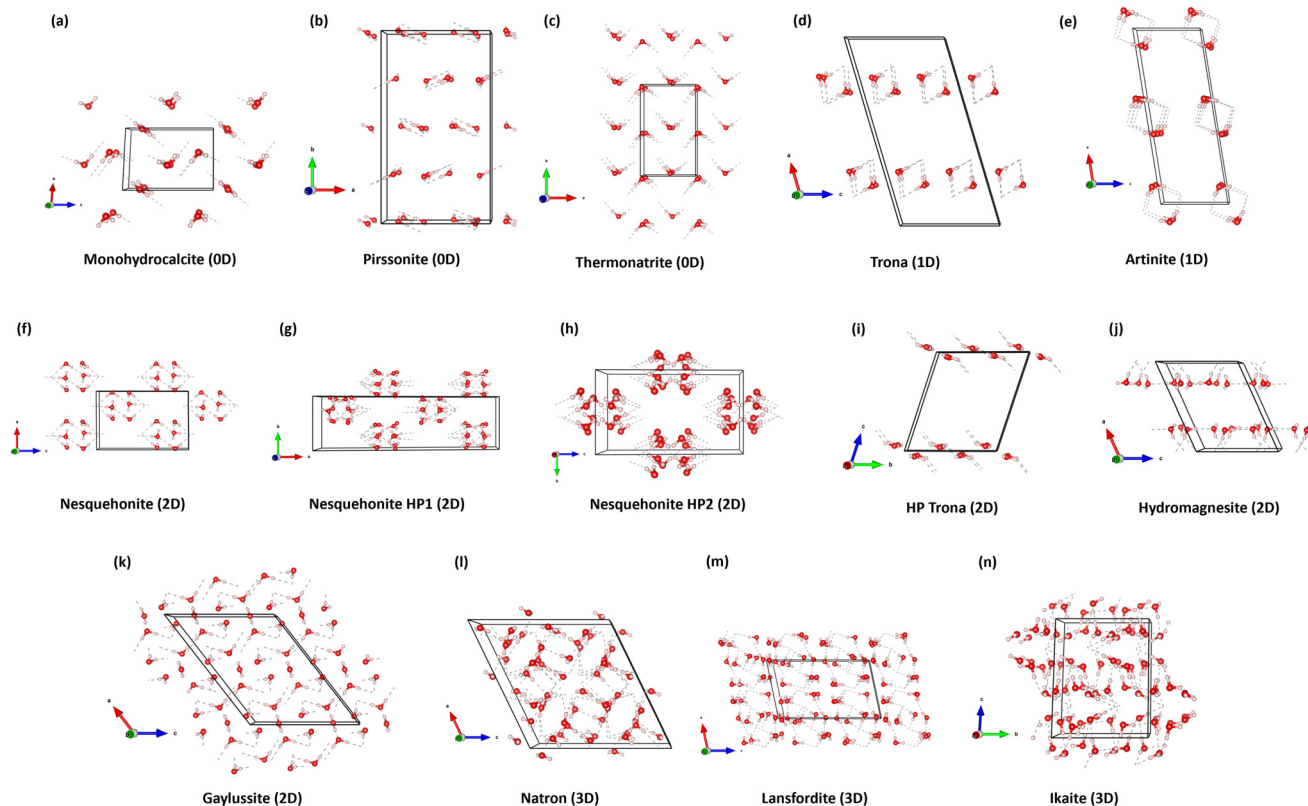
Fig. 10 Hydrogen bond networks of selected hydrated carbonates viewed along specific crystallographic axes: (a) monohydrocalcite, b-axis; (b) pirssonite, c-axis; (c) thermonatrite, c-axis; (d) trona, b-axis; (e) artinite, b-axis; (f) nesquehonite, b-axis; (g) nesquehonite HP1, b-axis; (h) nesquehonite HP2, a-axis; (i) HP trona, a-axis; (j) hydromagnesite, b-axis; (k) gaylussite, b-axis; (l) natron, b-axis; (m) lansfordite, b-axis; and (n) ikaite, a-axis. Oxygen (O) and hydrogen (H) atoms are shown in red and white, respectively.

characterized by isolated hydrogen-bonded clusters, in which water molecules interact primarily within their immediate coordination environments, without establishing extended connectivity across the lattice. The 1D category includes trona and artinite, illustrated in Fig. 10d and e, respectively, in which hydrogen bonds form chain-like motifs along a single crystallographic direction. In these cases, water molecules typically bridge adjacent carbonate groups or cations, giving rise to extended one-dimensional hydrogen-bonded ribbons. 2D hydrogen-bond networks are found in nesquehonite and its high-pressure polymorphs, HP trona, hydromagnesite, and gaylussite, illustrated in Fig. 10f, g, h, i, j and k, respectively. In these minerals, hydrogen bonds form either multiple chains or continuous layers within a specific crystallographic plane, interconnecting structural units and enhancing interchain and interlayer cohesion. Minerals such as natron, lansfordite, and ikaite, illustrated in Fig. 10l, m and n, respectively, exhibit 3D (framework) hydrogen-bond networks, characterized by a fully interconnected system of hydrogen bonds extending in all three spatial directions. It is worth noting that ikaite represents a special case within the 3D category, as its hydrogen-bond network also features cage-like motifs, in which water molecules form closed clusters surrounding cations and carbonate groups. This special configuration plays a critical role in the stabilization of its low-temperature phase. This arrangement has been noted in the literature as structurally significant, as high-pressure conditions are expected to stabilize ikaite; indeed, the volume occupied by ikaite is approximately 20% less than that of an equivalent mixture of $CaCO_3$ and six water molecules.[98]

There is a systematic trend in hydrogen-bond dimensionality across hydrated carbonates, although it is not strictly linear. The degree of hydration facilitates the formation of more extended hydrogen-bond networks, resulting in higher-dimensional connectivity. For instance, a low degree of hydration ($1–2H_2O$) tends to support 0D networks, where hydrogen bonding is limited to isolated water clusters. A moderate degree of hydration ($2–3H_2O$) typically supports 1D networks, in which water molecules bridge adjacent polyhedral chains. Moderate to high hydration levels ($3–5H_2O$) may give rise to 2D networks, where water molecules link layers of carbonate groups and cation-centered polyhedra. An exception to this pattern is high-pressure (HP) trona, which illustrates how elevated pressure conditions alter the fundamental chemistry of solids. Under compression, atomic interactions become increasingly repulsive, promoting structural rearrangements and phase transitions that reduce the system's free energy. These changes can lead to localized, layer-like hydrogen-bond networks despite the mineral's high-water content.[99–101] The formation of three-dimensional (3D) hydrogen-bond networks appears to require a high degree of hydration ($\geq 5H_2O$).

Ultimately, the dimensionality of hydrogen-bond networks arises not solely from hydration level but from the interplay among water content, cation coordination environment, crystallographic symmetry, and structural topological flexibility. While the observed trends provide useful insight, further studies—particularly those focused on phases with intermediate stoichiometries—are needed to fully elucidate the relationship between hydration and H-bond dimensionality.

Nonetheless, a consistent feature among all analyzed carbonates is the predominance of ionic hydrogen bonds exhibiting moderate but systematic directionality. This characteristic is preserved regardless of hydration degree, crystal structure, presence of hydroxyl or bicarbonate groups, or the coordination geometry of the metal cation, which ranges from $[MO_6]$ to $[MO_8]$ polyhedra.

Applications of nesquehonite

Nesquehonite and other HMCs have a wide range of applications. Industrial uses include pharmaceuticals, cosmetic manufacturing, the rubber industry, filter materials, and lithographic inks, as well as serving as precursors for other magnesium-based chemicals. In geological and environmental contexts, they are particularly relevant for carbon capture and sequestration (CCS)—the most prominent and widely studied application—and can also be used as cementitious materials.[24,34,43,102] Some of the numerous applications of nesquehonite will be presented in this section.

The production and release of metal-rich drainage during carbon mineralization may lead to both on-site and off-site contamination of surface waters, groundwater, soils, and sediments under various implementation scenarios. As a primary mineral product of carbon mineralization reactions at Earth's surface, nesquehonite and other hydrated Mg-carbonate minerals may serve as important—and previously unrecognized—sinks for mobilized trace metals. Hamilton et al.[103] demonstrated nesquehonite's capacity to sequester trace metals such as chromium (Cr), nickel (Ni), manganese (Mn), cobalt (Co), and copper (Cu) through substitution for Mg^{2+} in the crystal structure. This finding indicates that nesquehonite can act as an effective crystal trap for transition metals, suggesting its potential as a relatively long-term and stable storage option.

Reactive magnesia cement (RMC) is considered an effective alternative to Portland cement (PC) in the search for sustainable cementitious materials with a lower carbon footprint, due to its lower calcination temperature. The strength development of RMC depends on the hydration of MgO to form $Mg(OH)_2$, followed by carbonation of $Mg(OH)_2$, which produces a series of crystalline hydrated magnesium carbonates (HMCs) and amorphous magnesium carbonate phases. These HMCs form interconnected microstructural networks within the hardened RMC, reducing porosity and significantly improving its strength. Li et al.[104] demonstrated that the inclusion of nesquehonite at dosages below 1 wt% enhanced both hydration and carbonation, leading to reduced porosity and improved early and final compressive

strength of RMC. However, dosages above 1 wt% inhibited MgO hydration. Shi et al.[106] further showed that, regardless of whether the cement was cured in air or in water, the addition of nesquehonite increased the compressive strength of MgO paste. Under air curing, the maximum strength reached 9 MPa for a sample containing 4.14 wt% nesquehonite after 28 days, compared to 6 MPa for pure MgO under the same conditions. Under water curing, samples with 4.14 wt% and 7.87 wt% nesquehonite exhibited approximately the same maximum strength of 5 MPa, in contrast to 1.5 MPa for pure MgO. Later, Montserrat-Torres, Winnefeld, and Lothenbach[105] reported similar effects at higher concentrations: after 28 days, an inclusion of 50 wt% nesquehonite resulted in compressive strengths of 43–44 MPa. Their study also demonstrated that the flexural strength was independent of the nesquehonite dosage, improving from 2 MPa in pure MgO to 5–6 MPa regardless of the amount added.

Current global warming and climate change have raised numerous concerns, particularly regarding the reduction of anthropogenic CO_2 emissions and the stabilization of this greenhouse gas's concentration in the atmosphere. CCS is a promising approach, especially through its sequestration in a stable mineral form over long periods via mineral carbonation. However, making long-term predictions about the safety of underground CO_2 storage remains challenging. Complementary CCS technologies that promote CO_2 sequestration through the neoformation of carbonates offer permanent and safe storage, as these carbonates are thermodynamically stable under ambient conditions. This natural process has formed the vast carbonate rock deposits found on Earth's surface. The interaction between alkaline earth metal ions and CO_2 in aqueous solution favors the precipitation of calcium and magnesium carbonates. Focusing on magnesium offers an advantage because Mg carbonates contain approximately 21% more CO_2 by weight compared to calcium carbonates. Nesquehonite presents several advantages that make its application attractive.[24,39,107–109] However, its direct application for this purpose is not yet fully established. Ongoing research aims to better understand key aspects of nesquehonite's behavior to enable more effective and targeted applications. For example, Ferrini et al.[38] experimentally demonstrated that the application of nesquehonite in the CCS process offers several advantages: the process is kinetically favored and straightforward; nesquehonite forms in a very short time; it is a chemically stable solid product, enabling long-term CO_2 storage; the starting reactants are locally abundant, providing the potential for a cost-effective niche in CO_2 sequestration via mineralization; and nesquehonite can potentially be used for industrial purposes, with its disposal near the surface or underground posing limited environmental risks. Meanwhile, Pokharel et al.[110] investigated the formation, stability, and phase transformations of nesquehonite in the presence of dissolved silica. On the other hand, several authors[38,39,41] demonstrated that nesquehonite remains stable up to 323 K,

suggesting that it can serve as a CO_2-sequestering medium under typical surface temperature conditions on Earth. Their work provides valuable insights into the thermal behavior of nesquehonite. In addition to that, the studies by Santamaría-Pérez et al.[24] and Botan-Neto et al.[71] have explored the $P–T$ phase diagram, the equation of state and the anisotropy at different thermodynamic conditions, assessing the structural stability of nesquehonite under pressures and temperatures well above those with practical applications in CCS technologies. These studies, however, determine the mechanical properties and the systematic crystallochemical behavior of this compound. To effectively model CO_2 mineral trapping within this mineral, it is essential to develop a comprehensive understanding of its thermal, kinetic, structural, and mechanical properties, as well as synthesis conditions and morphological behavior. Such knowledge offers critical information for advancing CO_2 storage using nesquehonite in industrial applications and may support more accurate modeling of CO_2 sequestration in hydrated Mg-carbonate minerals.

Conclusions

This work provides a comprehensive review of the investigation on nesquehonite ($MgCO_3\cdot3H_2O$), motivated by its geological abundance, stability, and pivotal role within the $MgO–CO_2–H_2O$ system. We have revisited the different synthesis routes and morphological characteristics of nesquehonite, emphasizing the influence of additives on crystal growth and morphology. Thermal stability was thoroughly assessed via thermogravimetric and differential thermal analyses, revealing distinct dehydration steps and intermediate phases, with particular attention to the debated nature of the dehydration products.

High-pressure synchrotron X-ray diffraction experiments identified two pressure-induced polymorphs, HP1 and HP2, with their structural evolution and transition pressures validated by density functional theory calculations. Complementary high-temperature experiments under pressure confirmed the formation of a unique thermal phase preceding the decomposition into magnesite. Raman spectroscopy under compression provided additional insights into vibrational behavior and phase stability of the polymorphs, supporting the observed transitions.

Hydrogen bonding analysis demonstrated predominantly ionic and moderately directional interactions, consistent across nesquehonite and related hydrated carbonates, irrespective of structural complexity or hydration state. Additionally, a comparative evaluation with minerals exhibiting distinct structural motifs was conducted, addressing the role of "lattice" water molecules in nesquehonite and the diversity of cation coordination geometries.

Finally, the study highlights the significant potential of nesquehonite in applications ranging from CO_2 mineralization to materials science and sustainable

cementitious technologies. Its favorable kinetics, thermodynamic stability, and structural characteristics position nesquehonite as a promising candidate for environmentally relevant processes.

In summary, this integrated experimental and theoretical overview establishes a clear and accessible framework for understanding nesquehonite's structure, properties, and phase behavior, thereby providing valuable insights for further research across multiple scientific domains.

Conflicts of interest

There are no conflicts to declare.

Data availability

No primary research results, software or code have been included and no new data were generated or analyzed as part of this review.

Acknowledgements

References

1 R. Dasgupta, Ingassing, Storage, and Outgassing of Terrestrial Carbon through Geologic Time, *Rev. Mineral. Geochem.*, 2013, **75**, 183–229.

2 R. M. Hazen and C. M. Schiffries, Why Deep Carbon?, *Rev. Mineral. Geochem.*, 2013, **75**, 1–6.

3 Y. Liu, C. Chen, D. He and W. Chen, Deep carbon cycle in subduction zones, *Sci. China: Earth Sci.*, 2019, **62**, 1764–1782.

4 R. Dasgupta and M. M. Hirschmann, The deep carbon cycle and melting in Earth's interior, *Earth Planet. Sci. Lett.*, 2010, **298**, 1–13.

5 M. Isshiki, T. Irifune, K. Hirose, S. Ono, Y. Ohishi, T. Watanuki, E. Nishibori, M. Takata and M. Sakata, Stability of magnesite and its high-pressure form in the lowermost mantle, *Nature*, 2004, **427**, 60–63.

6 S. Arapan and R. Ahuja, High-pressure phase transformations in carbonates, *Phys. Rev. B: Condens. Matter Mater. Phys.*, 2010, **82**, 184115.

7 X. Yuan, X. Xiong, G. Zhang and R. A. Mayanovic, Application of calcite, Mg-calcite, and dolomite as Raman pressure sensors for high-pressure, high-temperature studies, *J. Raman Spectrosc.*, 2020, **51**, 1248–1259.

8 D. Pan and G. Galli, The fate of carbon dioxide in water-rich fluids under extreme conditions, *Sci. Adv.*, 2016, **2**(10), e1601278.

9 H. Effenberger, K. Mereiter, J. Zemann and S. Dolomite, Crystal structure refinements of magnesite, calcite, rhodochrosite, siderite, smithonite, and dolomite, with discussion of some aspects of the stereochemistry of calcite type carbonates, *Z. Kristallogr.*, 1981, **156**, 233–243.

10 B. Nashar, Barringtonite—A new hydrous magnesium carbonate from Barrington Tops, New South Wales, Australia, *Mineral. Mag. J. Mineral. Soc.*, 1965, **34**, 370–372.

11 G. W. Stephan and C. H. MacGillavry, The crystal structure of nesquehonite, $MgCO_3.3H_2O$, *Acta Crystallogr., Sect. B*, 1972, **28**, 1031–1033.

12 R. J. Hill, J. H. Canterford and F. J. Moyle, New data for lansfordite, *Mineral. Mag.*, 1982, **46**, 453–457.

13 M. Akao, F. Marumo and S. Iwai, The crystal structure of hydromagnesite, *Acta Crystallogr., Sect. B*, 1974, **30**, 2670–2672.

14 J. H. Canterford, G. Tsambourakis and B. Lambert, Some observations on the properties of dypingite, $Mg_5(CO_3)_4(OH)_2 \cdot 5H_2O$, and related minerals, *Mineral. Mag.*, 1984, **48**, 437–442.

15 J. Suzuki and M. Ito, A new magnesium carbonate hydrate mineral, $Mg_5(CO_3)_4(OH)_2 \bullet 8H_2O$, *Ganseki Kobutsu Kosho Gakkaishi*, 1973, **68**, 353–361.

16 G. Raade, Dypingite, a new hydrous basic carbonate of magnesium, from Norway, *Am. Mineral.*, 1970, **55**, 1457–1465.

17 P. M. de Wolff, The crystal structure of artinite, $Mg_2(OH)_2CO_3.3H_2O$, *Acta Crystallogr.*, 1952, **5**, 286–287.

18 C. Rincke, H. Schmidt and W. Voigt, A new hydrate of magnesium carbonate, $MgCO_3 \cdot 6H_2O$, *Acta Crystallogr., Sect. C: Struct. Chem.*, 2020, **76**, 244–249.

19 J. T. Kloprogge, W. N. Martens, L. Nothdurft, L. V. Duong and G. E. Webb, Low temperature synthesis and characterization of nesquehonite, *J. Mater. Sci. Lett.*, 2003, **22**, 825–829.

20 A. Kastrinakis, V. Skliros, P. Tsakiridis and M. Perraki, in *International Conference on Raw Materials and Circular Economy*, MDPI, Basel Switzerland, 2021, p. 60.

21 F. A. Genth and S. L. Penfield, On Lansfordite, nesquehonite, a new mineral, and pseudomorphs of nesquehonite after lansfordite, *Am. J. Sci.*, 1890, **39**, 121–137.

22 J. D. Dunitz, The interpretation of pseudo-orthorhombic diffraction patterns, *Acta Crystallogr.*, 1964, **17**, 1299–1304.

23 G. Jauffret, J. Morrison and F. P. Glasser, On the thermal decomposition of nesquehonite, *J. Therm. Anal. Calorim.*, 2015, **122**, 601–609.

24 D. Santamaría-Pérez, R. Chuliá-Jordán, J. Gonzalez-Platas, A. Otero-de-la-Roza, J. Ruiz-Fuertes, J. Pellicer-Porres, R. Oliva and C. Popescu, Polymorphism and Phase Stability of Hydrated Magnesium Carbonate Nesquehonite $MgCO_3 \cdot 3H_2O$: Negative Axial Compressibility and Thermal Expansion in a Cementitious Material, *Cryst. Growth Des.*, 2024, **24**, 1159–1169.

25 D. Langmuir, Stability of Carbonates in the System MgO-CO$_2$-H$_2$O, *J. Geol.*, 1965, **73**, 730–754.

26 E. Königsberger, L.-C. Königsberger and H. Gamsjäger, Low-temperature thermodynamic model for the system Na$_2$CO$_3$–MgCO$_3$–CaCO$_3$–H$_2$O, *Geochim. Cosmochim. Acta*, 1999, **63**, 3105–3119.

27 M. Hänchen, V. Prigiobbe, R. Baciocchi and M. Mazzotti, Precipitation in the Mg-carbonate system—effects of temperature and CO$_2$ pressure, *Chem. Eng. Sci.*, 2008, **63**, 1012–1028.

28 I. M. Power, P. A. Kenward, G. M. Dipple and M. Raudsepp, Room Temperature Magnesite Precipitation, *Cryst. Growth Des.*, 2017, **17**, 5652–5659.

29 G. D. Saldi, G. Jordan, J. Schott and E. H. Oelkers, Magnesite growth rates as a function of temperature and saturation state, *Geochim. Cosmochim. Acta*, 2009, **73**, 5646–5657.

30 F. L. Sayles and W. S. Fyfe, The crystallization of magnesite from aqueous solution, *Geochim. Cosmochim. Acta*, 1973, **37**, 87–99.

31 S. Guermech, J. Mocellin, L.-H. Tran, G. Mercier and L.-C. Pasquier, A study of hydromagnesite and nesquehonite precipitation in indirect aqueous carbonation of thermally-activated serpentine in a batch mode, *J. Cryst. Growth*, 2022, **584**, 126540.

32 C. L. Christ and P. B. Hostetler, Studies in the System MgO-SiO$_2$-CO$_2$-H$_2$O (II): The Activity-Product Constant of Magnesite, *Am. J. Sci.*, 1970, **268**, 439–453.

33 H. Dong, C. Unluer, E.-H. Yang, F. Jin and A. Al-Tabbaa, Microstructure and carbon storage capacity of hydrated magnesium carbonates synthesized from different sources and conditions, *J. CO$_2$ Util.*, 2019, **34**, 353–361.

34 G. Yamamoto, A. Kyono, J. Abe, A. Sano-Furukawa and T. Hattori, Crystal structure of nesquehonite, MgCO$_3$·3H(D)$_2$O by neutron diffraction and effect of pH on structural formulas of nesquehonite, *J. Mineral. Petrol. Sci.*, 2021, **116**, 96–103.

35 D. W. Ming and W. T. Franklin, Synthesis and Characterization of Lansfordite and Nesquehonite, *Soil Sci. Soc. Am. J.*, 1985, **49**, 1303–1308.

36 A. V. Kazakov, M. M. Tikhomirova and V. I. Plotnikova, The system of carbonate equilibria, *Int. Geol. Rev.*, 1959, **1**, 1–39.

37 W. Cheng and Z. Li, Precipitation of nesquehonite from homogeneous supersaturated solutions, *Cryst. Res. Technol.*, 2009, **44**, 937–947.

38 V. Ferrini, C. De Vito and S. Mignardi, Synthesis of nesquehonite by reaction of gaseous CO$_2$ with Mg chloride solution: Its potential role in the sequestration of carbon dioxide, *J. Hazard. Mater.*, 2009, **168**, 832–837.

39 P. Ballirano, C. De Vito, V. Ferrini and S. Mignardi, The thermal behaviour and structural stability of nesquehonite, MgCO$_3$·3H$_2$O, evaluated by in situ laboratory parallel-beam X-ray powder diffraction: New constraints on CO$_2$ sequestration within minerals, *J. Hazard. Mater.*, 2010, **178**, 522–528.

40 M. Dong, W. Cheng, Z. Li and G. P. Demopoulos, Solubility and Stability of Nesquehonite (MgCO$_3$·3H$_2$O) in NaCl, KCl, MgCl$_2$, and NH$_4$Cl Solutions, *J. Chem. Eng. Data*, 2008, **53**, 2586–2593.

41 M. Xu, S. Yao, Y. Gao, Y. Bai, J. Teng, W. Liu, W. Cui, Z. Meng and P. Yan, Polymorphism and thermal stability of nesquehonite (MgCO$_3$·3H$_2$O) regulated by magnesium L-aspartate: For CO$_2$ mineral sequestration, *Thermochim. Acta*, 2025, **744**, 179920.

42 P. J. Davies and B. Bubela, The transformation of nesquehonite into hydromagnesite, *Chem. Geol.*, 1973, **12**, 289–300.

43 Z. Zhang, Y. Zheng, Y. Ni, Z. Liu, J. Chen and X. Liang, Temperature- and pH-Dependent Morphology and FT−IR Analysis of Magnesium Carbonate Hydrates, *J. Phys. Chem. B*, 2006, **110**, 12969–12973.

44 V. Vágvölgyi, M. Hales, R. L. Frost, A. Locke, J. Kristóf and E. Horváth, Conventional and controlled rate thermal analysis of nesquehonite Mg(HCO$_3$)(OH)·2(H$_2$O), *J. Therm. Anal. Calorim.*, 2008, **94**, 523–528.

45 N. Sutradhar, A. Sinhamahapatra, S. K. Pahari, P. Pal, H. C. Bajaj, I. Mukhopadhyay and A. B. Panda, Controlled Synthesis of Different Morphologies of MgO and Their Use as Solid Base Catalysts, *J. Phys. Chem. C*, 2011, **115**, 12308–12316.

46 A. A. Park, R. Jadhav and L. Fan, CO$_2$ Mineral Sequestration: Chemically Enhanced Aqueous Carbonation of Serpentine, *Can. J. Chem. Eng.*, 2003, **81**, 885–890.

47 A. L. Harrison, I. M. Power and G. M. Dipple, Accelerated Carbonation of Brucite in Mine Tailings for Carbon Sequestration, *Environ. Sci. Technol.*, 2013, **47**, 126–134.

48 G. L. Smithson and N. N. Bakhshi, Kinetics and Mechanism of Carbonation of Magnesium Oxide Slurries, *Ind. Eng. Chem. Process Des. Dev.*, 1973, **12**, 99–106.

49 K. Mitsuhashi, N. Tagami, K. Tanabe, T. Ohkubo, H. Sakai, M. Koishi and M. Abe, Synthesis of Microtubes with a Surface of "House of Cards" Structure via Needlelike Particles and Control of Their Pore Size, *Langmuir*, 2005, **21**, 3659–3663.

50 H. T. Schaef, C. F. Windisch, B. P. McGrail, P. F. Martin and K. M. Rosso, Brucite [Mg(OH$_2$)] carbonation in wet supercritical CO$_2$: An in situ high pressure X-ray diffraction study, *Geochim. Cosmochim. Acta*, 2011, **75**, 7458–7471.

51 L. Zhao, L. Sang, J. Chen, J. Ji and H. H. Teng, Aqueous Carbonation of Natural Brucite: Relevance to CO$_2$ Sequestration, *Environ. Sci. Technol.*, 2010, **44**, 406–411.

52 L. Hopkinson, P. Kristova, K. Rutt and G. Cressey, Phase transitions in the system MgO–CO$_2$–H$_2$O during CO$_2$ degassing of Mg-bearing solutions, *Geochim. Cosmochim. Acta*, 2012, **76**, 1–13.

53 J. T. Kloprogge, W. N. Martens, L. Nothdurft, L. V. Duong and G. E. Webb, Low temperature synthesis and characterization of nesquehonite, *J. Mater. Sci. Lett.*, 2003, **22**, 825–829.

54 A. Yahyazadeh, A. F. Mofrad, E. Yahyazadeh, M. Outokesh, S. M. Safavi, S. Kazzazi, N. Madani and B. B. Hesari, A chronological study on formation mechanism of nesquehonite from nanoparticles to grown crystals and its application in nanoparticle synthesis, *Sci. Rep.*, 2025, **15**, 20956.

55 J. Back, A. Ismailov, H. Sreenivasan, J.-H. Smått, H. S. Santos, H. Nguyen, E. Levänen, R. Zevenhoven and P. Kinnunen, Influence of additives, temperature, and pressure on the morphology of nesquehonite– results from three synthesis routes, *Emergent Mater.*, 2025, **8**, 2853–2868.

56 L. Hopkinson, K. Rutt and G. Cressey, The Transformation of Nesquehonite to Hydromagnesite in the System CaO-MgO-H$_2$O-CO$_2$: An Experimental Spectroscopic Study, *J. Geol.*, 2008, **116**, 387–400.

57 E. J. Swanson, K. J. Fricker, M. Sun and A.-H. A. Park, Directed precipitation of hydrated and anhydrous magnesium carbonates for carbon storage, *Phys. Chem. Chem. Phys.*, 2014, **16**, 23440–23450.

58 R. M. Dell and S. W. Weller, The thermal decomposition of nesquehonite MgCO$_3$· 3H$_2$O and magnesium ammonium carbonate MgCO$_3$·(NH$_4$)$_2$CO$_3$·4H$_2$O, *Trans. Faraday Soc.*, 1959, **55**, 2203–2220.

59 B. Morgan, S. Wilson, I. C. Madsen, Y. M. Gozukara and J. Habsuda, Increased thermal stability of nesquehonite (MgCO$_3$·3H$_2$O) in the presence of humidity and CO$_2$: Implications for low-temperature CO$_2$ storage, *Int. J. Greenhouse Gas Control*, 2015, **39**, 366–376.

60 R. L. Frost, M. C. Hales and W. N. Martens, Thermogravimetric analysis of selected group (II) carbonateminerals — Implication for the geosequestration of greenhouse gases, *J. Therm. Anal. Calorim.*, 2009, **95**, 999–1005.

61 H. Ren, Z. Chen, Y. Wu, M. Yang, J. Chen, H. Hu and J. Liu, Thermal characterization and kinetic analysis of nesquehonite, hydromagnesite, and brucite, using TG–DTG and DSC techniques, *J. Therm. Anal. Calorim.*, 2014, **115**, 1949–1960.

62 V. Vágvölgyi, R. L. Frost, M. Hales, A. Locke, J. Kristóf and E. Horváth, Controlled rate thermal analysis of hydromagnesite, *J. Therm. Anal. Calorim.*, 2008, **92**, 893–897.

63 J. Lanas and J. I. Alvarez, Dolomitic lime: thermal decomposition of nesquehonite, *Thermochim. Acta*, 2004, **421**, 123–132.

64 X. Tao, J. Xu, K. Yang and D. Lin, Novel oxymagnesite/green rust nanohybrids for selective removal and slow release of phosphate in water, *Sci. Total Environ.*, 2023, **856**, 159207.

65 S. Frykstrand, C. Strietzel, J. Forsgren, J. Ångström, V. Potin and M. Strømme, Synthesis, electron microscopy and X-ray characterization of oxymagnesite, MgO·2MgCO$_3$, formed from amorphous magnesium carbonate, *CrystEngComm*, 2014, **16**, 10837–10844.

66 K. Watabe, Y. Seto and H. Miura, Crystal Structure of 3MgO·2CO$_2$ Solved by Monte Carlo Simulation, *J. Comput. Chem., Jpn.*, 2009, **8**, 179–182.

67 A. M. Chaka and A. R. Felmy, Ab Initio Thermodynamic Model for Magnesium Carbonates and Hydrates, *J. Phys. Chem. A*, 2014, **118**, 7469–7488.

68 R. Boehler, Diamond cells and new materials, *Mater. Today*, 2005, **8**, 34–42.

69 D. Santamaría-Pérez, L. Gracia, G. Garbarino, A. Beltrán, R. Chuliá-Jordán, O. Gomis, D. Errandonea, Ch. Ferrer-Roca, D. Martínez-García and A. Segura, High-pressure study of the behavior of mineral barite by x-ray diffraction, *Phys. Rev. B: Condens. Matter Mater. Phys.*, 2011, **84**, 054102.

70 K. Glazyrin, S. Khandarkhaeva, T. Fedotenko, W. Dong, D. Laniel, F. Seiboth, A. Schropp, J. Garrevoet, D. Brückner, G. Falkenberg, A. Kubec, C. David, M. Wendt, S. Wenz, L. Dubrovinsky, N. Dubrovinskaia and H.-P. Liermann, Sub-micrometer focusing setup for high-pressure crystallography at the Extreme Conditions beamline at PETRA III, *J. Synchrotron Radiat.*, 2022, **29**, 654–663.

71 B. D. Botan-Neto, D. Santamaria-Perez, L. Bayarjargal, E. Bykova, J. Gonzalez-Platas and A. Otero-de-la-Roza, Dense Hydrated Magnesium Carbonate MgCO$_3$·3H$_2$O Phases, *Inorg. Chem.*, 2024, **63**, 15762–15771.

72 L. Borromeo, N. Egeland, M. W. Minde, U. Zimmermann, S. Andò, M. V. Madland and R. I. Korsnes, Quick, easy, and economic mineralogical studies of flooded chalk for EOR experiments using Raman spectroscopy, *Minerals*, 2018, **8**, 221.

73 H. G. M. Edwards, S. E. J. Villar, J. Jehlicka and T. Munshi, FT–Raman spectroscopic study of calcium-rich and magnesium-rich carbonate minerals, *Spectrochim. Acta, Part A*, 2005, **61**, 2273–2280.

74 G. Montes-Hernandez, Magnesite formation from nesquehonite slurry at 90 °C using some soluble Mg salts: Eitelite as an atypical transient mineral phase, *Chem. Eng. Sci.*, 2024, **287**, 119776.

75 V. Skliros, P. Tsakiridis and M. Perraki, A combined Raman, Fourier transform infrared, and X-ray diffraction study of thermally treated nesquehonite, *J. Raman Spectrosc.*, 2020, **51**, 1445–1453.

76 A. Y. Likhacheva, S. Miloš, A. V. Romanenko, S. V. Goryainov, A. I. Semerikova, S. V. Rashchenko, R. Miletich and A. Shatsky, High-pressure behavior and stability of synthetic buetschliite K$_2$Ca(CO$_3$)$_2$ up to 19 GPa and 300°C, *J. Raman Spectrosc.*, 2024, **55**(4), 517–524.

77 M. C. Hales, R. L. Frost and W. N. Martens, Thermo-Raman spectroscopy of synthetic nesquehonite - Implication for the geosequestration of greenhouse gases, *J. Raman Spectrosc.*, 2008, **39**, 1141–1149.

78 T. Steiner, The Hydrogen Bond in the Solid State, *Angew. Chem., Int. Ed.*, 2002, **41**, 48–76.

79 G. C. Pimentel and A. L. McClellan, Hydrogen Bonding, *Annu. Rev. Phys. Chem.*, 1971, **22**, 347–385.

80 S. J. Grabowski, What Is the Covalency of Hydrogen Bonding?, *Chem. Rev.*, 2011, **111**, 2597–2625.

81 P. A. Hunt, C. R. Ashworth and R. P. Matthews, Hydrogen bonding in ionic liquids, *Chem. Soc. Rev.*, 2015, **44**, 1257–1288.

82 S. J. Grabowski and J. Leszczynski, *Hydrogen Bonding—New Insights*, Springer Netherlands, 2006.

83 G. A. Jeffrey, *An Introduction to Hydrogen Bonding*, Oxford University Press, New York, 1997.

84 F. Nestola, A. V. Kasatkin, S. S. Potapov, O. Y. A. Chervyatsova and A. Lanza, First crystal-structure determination of natural lansfordite, $MgCO_3 \cdot 5H_2O$, *Mineral. Mag.*, 2017, **81**, 1063–1071.

85 M. Akao and S. Iwai, The hydrogen bonding of artinite, *Acta Crystallogr., Sect. B*, 1977, **33**, 3951–3953.

86 H. Effenberger, Kristallstruktur und Infrarot-Absorptionsspektrum von synthetischem Monohydrocalcit, $CaCO_3 \cdot H_2O$, *Monatsh. Chem.*, 1981, **112**, 899–909.

87 K. F. Hesse, H. Küppers and E. Suess, Refinement of the structure of Ikaite, $CaCO_3 \cdot 6H_2O$, *Z. Kristallogr.*, 1983, **163**, 227–232.

88 K. K. Wu and I. D. Brown, A neutron diffraction study of $Na_2CO_3 \cdot H_2O$, *Acta Crystallogr., Sect. B*, 1975, **31**, 890–892.

89 E. Libowitzky and G. Giester, Washing soda (natron), $Na_2CO_3 \cdot 10H_2O$, revised: crystal structures at low and ambient temperatures, *Mineral. Petrol.*, 2003, **77**, 177–195.

90 E. O'Bannon, C. M. Beavers and Q. Williams, Trona at extreme conditions: A pollutant-sequestering material at high pressures and low temperatures, *Am. Mineral.*, 2014, **99**, 1973–1984.

91 B. D. Botan-Neto, D. Santamaria-Perez, L. Wedek, L. Bayarjargal, G. Bera, P. Botella, J. Pellicer-Porres, A. Otero-de-la-Roza, C. Popescu and F. G. Alabarse, Compressibility and Anisotropy of Trona: Unveiling the Structure of a Dense $Na_3H(CO_3)_2 \cdot 2H_2O$ Polymorph, *Inorg. Chem.*, 2025, **64**, 10067–10077.

92 A. M. Callegari and M. Boiocchi, High resolution X-ray diffraction data of pirssonite from Searles Lake, San Bernardino County, California, *Neues Jahrb. Mineral., Abh.*, 2013, **190**, 221–227.

93 B. Dickens and W. E. Brown, Crystal structures of $CaNa_2(CO_3)_2 \cdot 5H_2O$, synthetic gaylussite, and $CaNa_2(CO_3)_2 \cdot 2H_2O$, synthetic pirssonite, *Inorg. Chem.*, 1969, **8**, 2093–2103.

94 R. Demichelis, P. Raiteri and J. D. Gale, Structure of hydrated calcium carbonates: A first-principles study, *J. Cryst. Growth*, 2014, **401**, 33–37.

95 P. P. Kumar, A. G. Kalinichev and R. J. Kirkpatrick, Hydrogen-Bonding Structure and Dynamics of Aqueous Carbonate Species from Car–Parrinello Molecular Dynamics Simulations, *J. Phys. Chem. B*, 2009, **113**, 794–802.

96 S. S. Xantheas, Cooperativity and hydrogen bonding network in water clusters, *Chem. Phys.*, 2000, **258**, 225–231.

97 L. Zhao, K. Ma and Z. Yang, Changes of Water Hydrogen Bond Network with Different Externalities, *Int. J. Mol. Sci.*, 2015, **16**, 8454–8489.

98 A. R. Lennie, Ikaite ($CaCO_3.6H_2O$) compressibility at high water pressure: a synchrotron X-ray diffraction study, *Mineral. Mag.*, 2005, **69**, 325–335.

99 C.-S. Yoo, Chemistry under extreme conditions: Pressure evolution of chemical bonding and structure in dense solids, *Matter Radiat. Extremes*, 2020, **5**(1), 018202.

100 M. Miao, Y. Sun, E. Zurek and H. Lin, Chemistry under high pressure, *Nat. Rev. Chem.*, 2020, **4**, 508–527.

101 G. Shen and H. K. Mao, High-pressure studies with x-rays using diamond anvil cells, *Rep. Prog. Phys.*, 2017, **80**, 016101.

102 Q. Chen, T. Hui, H. Sun, T. Peng and W. Ding, Synthesis of magnesium carbonate hydrate from natural talc, *Open Chem.*, 2020, **18**, 951–961.

103 J. L. Hamilton, S. Wilson, B. Morgan, C. C. Turvey, D. J. Paterson, C. MacRae, J. McCutcheon and G. Southam, Nesquehonite sequesters transition metals and CO_2 during accelerated carbon mineralisation, *Int. J. Greenhouse Gas Control*, 2016, **55**, 73–81.

104 Z. Li, Z. Zhang, J. Qin, Y. Yue and J. Qian, Influence of nesquehonite seeds on hydration and carbonation of reactive magnesia cement, *Constr. Build. Mater.*, 2023, **409**, 134034.

105 P. Montserrat-Torres, F. Winnefeld and B. Lothenbach, Impact of nesquehonite on hydration and strength of MgO-based cements, *Cem. Concr. Res.*, 2025, **189**, 107772.

106 R. Shi, Y. Hao, D. Chen and W. Liu, Effect of Low Nesquehonite Addition on the Hydration Product and Pore Structure of Reactive Magnesia Paste, *Materials*, 2023, **16**, 2445.

107 C. De Vito, V. Ferrini, S. Mignardi, M. Cagnetti and F. Leccese, in *2012 11th International Conference on Environment and Electrical Engineering*, IEEE, 2012, pp. 323–327.

108 E. H. Oelkers, S. R. Gislason and J. Matter, Mineral Carbonation of CO_2, *Elements*, 2008, **4**, 333–337.

109 J. M. Matter and P. B. Kelemen, Permanent storage of carbon dioxide in geological reservoirs by mineral carbonation, *Nat. Geosci.*, 2009, **2**, 837–841.

110 R. Pokharel, I. C. Popa, Y. de Kok and H. E. King, Enhanced Nesquehonite Formation and Stability in the Presence of Dissolved Silica, *Environ. Sci. Technol.*, 2024, **58**, 362–370.